ESA Climate Change Initiative (CCI+)

Essential Climate Variable (ECV)

Antarctic_Ice_Sheet_cci+ (AIS_cci+)

End-to-end Uncertainty Budget (E3UB)

Prime & Science Lead: Andrew Shepherd

Northumbria University, Newcastle upon Tyne, United Kingdom

Technical Officer: Anna Maria Trofaier

ESA ECSAT, Didcot, United Kingdom

Consortium: DTU Microwaves and Remote Sensing Group (DTU-N)

DTU Geodynamics Group (DTU-S)

Environmental Earth Observation IT GmbH (ENVEO)

Deutsches Zentrum für Luft- und Raumfahrt (DLR) Remote Sensing Technology Institute (IMF)

Northumbria University (NU)

Science [&] Technology AS (ST)

Technische Universität Dresden (TUDr)

University College London (UCL/MSSL)

Signatures page

Prepared by	Jan Wuite Project Scientist, ENVEO	
Checked by	Andrew Shepherd Science Leader, NU	
Issued by	Daniele Fantin, Project Manager, S&T	Digitally signed by Daniele Fantin Date: 2025.02.10 14:59:40 CET
Approved by	Anna Maria Trofaier ESA Technical Officer	

Table of Contents

Change Log

Issue	Author	Affected Section	Change	Status
1.0	J. Wuite, ENVEO	All	Updated for Phase 2	Released to ESA
2.0	J. Wuite, ENVEO	All	Updated for Phase 2	Released to ESA

Acronyms and Abbreviations

Acronym	Explanation
AIS	Antarctic Ice Sheet
ADP	Algorithm Development Plan
AIS_cci+	Antarctic Ice Sheets CCI project Extension
API	Antarctic Peninsula
ATBD	Algorithm Theoretical Basis Document
CCI(+)	Climate Change Initiative (Extension)
CFL	Calving Front Location
CONAE	Comisión Nacional de Actividades Espaciales
DEM	Digital Elevation Model
DLR	Deutsches Zentrum für Luft- und Raumfahrt
DTU	Danish Technical University
EAIS	East Antarctic Ice Sheet
ECV	Essential Climate Variable
ENVEO	ENVironmental Earth Observation GmbH
EO	Earth Observation
ESA	European Space Agency
GLL	Grounding Line Location
GLM	Grounding Line Migration
GMB	Gravimetric Mass Balance
ISCL	Ice Shelf Coast Line
IV	Ice Velocity
IV-TCM	Ice Velocity Tidal Correction Module
IVC	Ice Velocity Change
MFID	Mass Flux Ice Discharge
MPC	Mission Performance Cluster
SEC	Surface Elevation Change
SOW	Statement of Work
ST	Science & Technology AS
TOPS	Terrain Observation by Progressive Scans
TUD	Technical University of Dresden
UB	University of Bristol
UCL	University College London
UN	University of Northumbria
WAIS	West Antarctic Ice Sheet
NASA	National Aeronautics and Space Administration
SAR	Synthetic Aperture Radar
InSAR	Interferometric SAR
ML	Machine Learning

1 Introduction

1.1 Purpose and Scope

This document contains the End-to-end Uncertainty Budget (E3UB) for the Antarctica_Ice_Sheet_cci (AIS_cci) project for CCI+ Phase 2, in accordance to contract and SoW [AD1 and AD2]. The central aim is to ascertain error characteristics that permit the identification of climate change over natural variability. The E3UB describes the end-to-end errors of ECV improvements, proposed for CCI+, and builds on the Phase 1 End-to-end Uncertainty Budget (E3UB) document [RD3] of the 'Antarctic_Ice_Sheet_cci+ project.

The overall error and uncertainty budget for products with new technical developments will be provided or re-assessed and updated where needed, considering errors induced by new sensors, models, corrections, technical developments, and continued validation/inter-comparison efforts, including Round Robin outcomes. The document describes the best current understanding of the sources of errors, and uncertainties for the retrieval algorithms of the parameters:

- Surface Elevation Change (SEC)
- Ice Velocity (IV)
- Ice Velocity Change (IVC)
- Grounding Line Location (GLL)
- Grounding Line Migration (GLM)
- Gravimetric Mass Balance (GMB)
- Ice Shelf CoastLines (ISCL)

1.2 Document Structure

This document is structured as follows:

- Chapter 1 provides an introduction to the document.
- Chapters 2 to 7 provide descriptions of end-to-end uncertainty budget for each ECV parameter.

1.3 Applicable and Reference Documents

Table 1.1: List of Applicable and Reference Documents

No	Doc. Id	Doc. Title	Date	Issue/ Revision/ Version
AD1	ESA/Contract No. 4000143397/23/I-NB CCI+ PHASE 2 - AIS	CCI+ PHASE 2 - NEW R&D ON CCI ECVS for AIS CCI	13.02.2024	NA
AD2	ESA-EOP-SC-AMT-2023-12 and its appendix 2	STATEMENT OF WORK, ESA EXPRESS PROCUREMENT – EXPRO CCI+ Phase 2 – Theme II – Antarctic Ice Sheet (AIS)	14.07.2023	1.2
AD3	ST-UL-ESA-AISCCI+-ATBD-002	Algorithm Theoretical Basis Document (ATBD)	07.02.2025	1.0
RD1	ST-UL-ESA-AISCCI+-E3UB-001	End-to-end Uncertainty Budget (E3UB)	20.05.2020	1.0
RD2	ST-UL-ESA-AISCCI-CECR-001	Comprehensive Error Characterisation Report (CECR)	04.07.2016	2.0

Note: If not provided, the reference applies to the latest released Issue/Revision/Version

2 Surface Elevation Change

2.1 Introduction

In this section the error sources, uncertainties, and methodology for characterisation of the errors of the derived surface elevation change from Ku-band radar altimetry and laser altimetry are outlined. Satellite radar and laser altimetry of ice sheets are characterized by a number of errors, some of which make their application for climate change measurements quite problematic, especially the problems of getting reliable data over the sloping coastal regions and outlet glaciers.

Table 2.1: Typical magnitude of errors in SEC.

Slope Correction	Corrects for slope-induced errors.	0 to 150
Retracking	Corrects for tracker lag.	-15 to 15
Tropospheric Refraction	Corrects for signal delay due to pressure variations and water vapour in the troposphere.	1.5 to 2.5
Ionospheric Refraction	Corrects for signal delay due to charged particles in the ionosphere.	.02 to .10
Tides (ocean and solid earth)	Removes earth and ocean dynamics.	-3 to 3
Ascending/descending bias	Biases between measurements on ascending and descending tracks	-2 to 2
Inter-satellite bias	Biases between measurements from different satellites	-2 to 3.5
Backscatter correction	Correction for dependence of elevation changes on changes in waveform parameters to correct variations in backscattering depth	±1.5 to ±3*

** Represents correction of elevation changes for the points of time series over grid cell. Range of correction depends on the correction method and applied retracking correction.*

2.2 Sources of error

The errors may be classified in a number of parameter groups, as outlined in the following subsections.

2.2.1 Instrument, orbit, and position errors

Pointing errors in pulse-limited RA is usually not an issue, as is the UTC timing of the satellite transmit and receive times, compared to the size of the radar footprint on the ground. Satellite orbit height errors for best post-processed orbits are typically 2-5 cm, and are, therefore, also not a major limitation issue in generating the essential climate variables (ECV) using radar or laser satellite altimetry . For the stability of the orbit and range measurement, the applications over ice sheets can benefit from the significant efforts made in calibrating and validating RA over oceans. A long-term stability at the cm-level has been demonstrated by several investigators in US and Europe across the ERS, Envisat and TOPEX missions (Faugere, 2007).

2.2.2 RA penetration into the firn

Radar penetration at Ku-band into the firm is a major limitation in RA, with volume scattering down to several meter depth dominating the long tail of the altimeter waveform. The location of the leading edge will be a function of the snow density distribution, and especially the presence of ice lenses in the snowpack (ice lenses form regularly in the intermediate percolation zone of the ice sheet, in connection with the yearly thaw-refreeze cycle). Ice lenses and buried sastrugi structures are suspected to be major sources of bias frequently seen between ascending and descending orbits e.g. see Wingham (2006) or Khovorostovsky (2012). The effect of penetration depth on the measured RA elevations is also dependent on the retracking method and thresholds chosen. Static penetration biases will cancel out during repeated SEC measurements, and time variant biases can be removed by performing a backscatter correction (Wingham et al., 1998). Laser altimeters track closer to the ice sheet surface because they operate at shorter wavelengths (Markus et al., 2017) that are observed to penetrate only tens of centimetres (Studinger et al., 2023). While they offer a more direct measurement of the ice sheet surface, they are more sensitive to short-term changes in height and laser altimeters are also impacted by cloud cover and drifting snow (Markus et al., 2017).

2.2.3 Range correction and retracking errors

The retracking and slope corrections are the dominant error source in ice sheet RA; geophysical corrections for ionospheric and atmospheric path delays are the source of additional errors, but are reasonably well understood and quantified from ocean RA. Choice of a robust retracker such as OCOG or TFMR is necessary for SEC estimation, as measurement density and precision over the whole ice sheet is more important than overall accuracy of measuring the snow-air interface. A trivial - but important - issue in RA is the use of a consistent reference system: TOPEX/Poseidon data do not refer to the same ellipsoid as the ERS/Envisat data. The difference of these systems is around 70 cm.

2.2.4 Errors due to surface slope and topography

The varying Antarctic topography (Figure 2.1) within the footprint of RA gives complicated return signal waveforms, and assigning the effective reflection point on the surface from the leading edge of the altimetric radar return waveform shape can be error prone and ambiguous, unless the radar instrument is especially designed for such surfaces (as in CryoSat-2's SARin mode). The spherical wave front of the pulse-limited radar pulse (used in ERS, ENVISAT and CryoSat-2's LRM mode) will – within the beam width of the radar pulse – have a first return from the nearest topography which can be significantly off (several km) from the satellite position on the ground. More recent missions such as Sentinel-3A, and 3-B use a delay-doppler (SAR) technique which delivers a 4-fold improvement in along track resolution (to ~300m), but its first return may be located up to 8km across track. Only CryoSat-2 is able to use interferometric techniques to locate the surface reflection in the across-track plane.

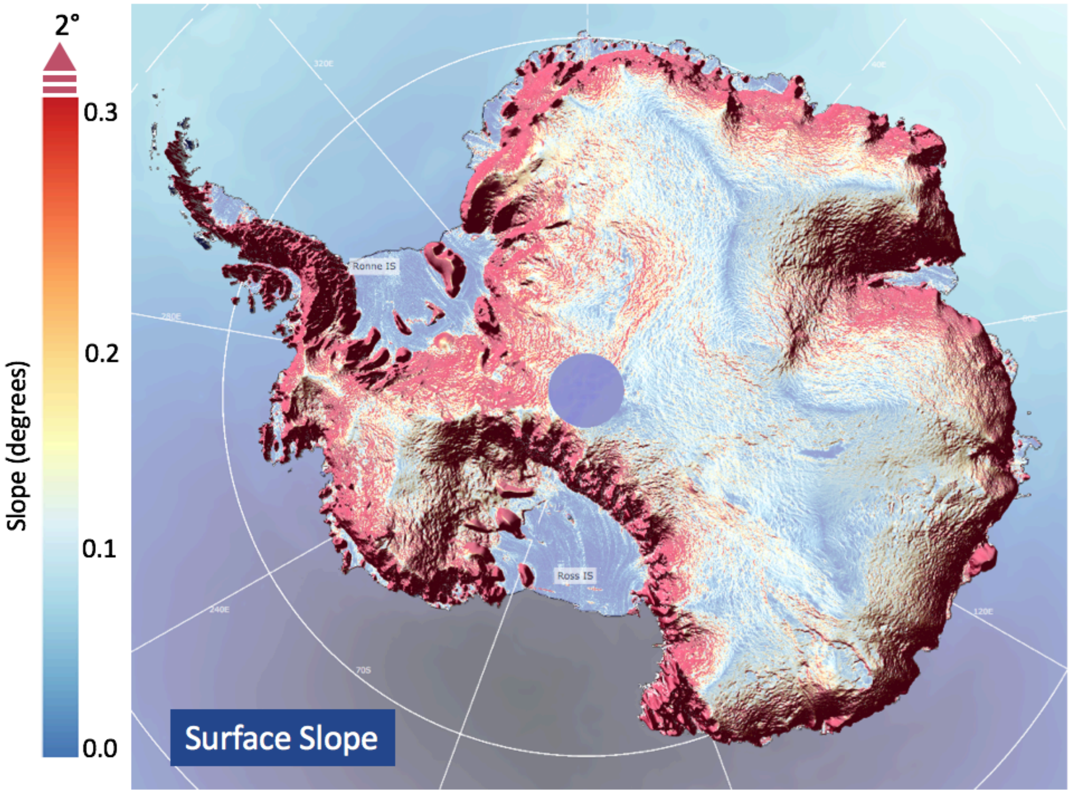

Figure 2.1: Surface Slope and Topographic Variability over Antarctica (Slope derived from CryoSat DEM, Slater, 2018)

Several methods for dealing with the problem of slope correction (for non-interferometric RA modes), have been proposed, e.g. Zwally (2015) or Brenner (1983), using either a correction for the off-nadir return assuming a linear sloping surface (keeping the ground reflection point at the satellite location), or relocating the orbit ground reflection point to the point of closest proximity using a DEM (moving the reflection point coordinates, and thus generating a "wiggly" non-equidistant trace of satellite reflection points instead of the regular satellite ground track). For a general review see Bamber, 1994. The spatial accuracy and resolution of the DEM, the time difference between the DEM and the measurement time, and relocation algorithm all effect the effectiveness of the slope correction. These are likely to improve over time and reduce the slope induced error.

Laser altimetry from ICESat and ICESat-2 does not have this limitation, due to the much narrower footprint (~70m,~17m respectively), but data are only available over cloud free areas during the period of 2003-2009 (ICESat) and from Oct 2018 (ICESat-2).

RA measurement precision is of primary importance for derivation of SEC, and the effect of slope on the precision can be measured by crossover analysis. For pulse limited RA (ERS, ENVISAT, CryoSat-2 LRM), Schröder et al. (2019) showed that the precision of RA measurements decreases with increasing surface slope (Figure 2.2), but the decrease can be mitigated with improvements in slope correction and by optimised retracking.

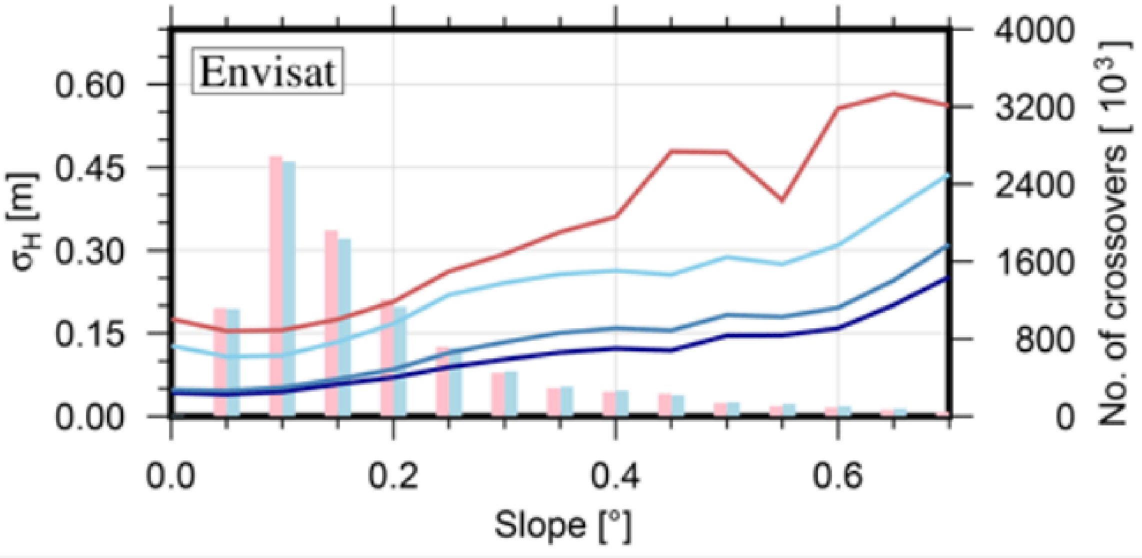

Figure 2.2: Precision of Envisat Measurements binned against slope (Schröder et al., (2019). The different curves correspond to different slope corrections and retracker thresholds.

Sentinel-3A, and 3-B's slope dependent SAR measurement precision over Antarctica has also been measured by McMillan et al. (2019) and by the S3 Mission Performance Center (S3MPC) (Figure 2.3), however the final performance of S3 over the higher slope regions is being rapidly improved with frequent baseline releases and will not be fully determined until a dedicated optimised full land ice reprocessing of the missions is performed in late 2020.

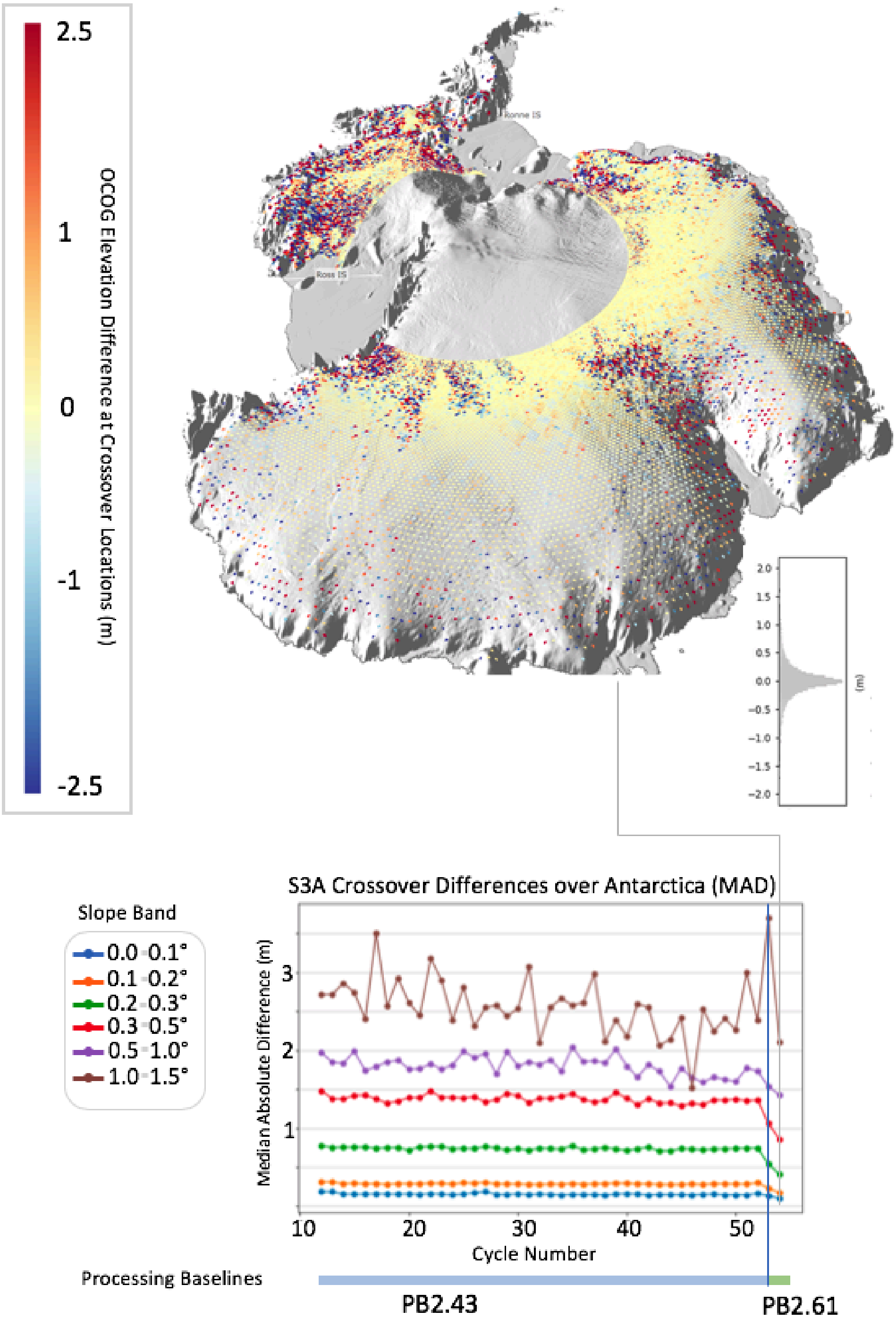

Figure 2.3: Precision of S3-A (OCOG retracker) for different bands of slope, showing improvements made in recent ESA processing baselines.

For CryoSat-2 in SARin mode over the Antarctic margins, a primary source of error is phase wrapping, and an incorrect detection of phase wrap can introduce errors of tens of meters. Phase ambiguity is currently detected (Figure 2.4) in the ESA products (baseline-D) but not corrected for.

The effect of slope and retracker type on CryoSat-2 SARin mode RA measurement precision over the Antarctic margins (a region of high slope and complex terrain) was also estimated by Schröder et al. (2019) in Figure 2.5. Although the slope-induced RA error can be very large, the effect on surface elevation change (SEC) is only a second order effect.

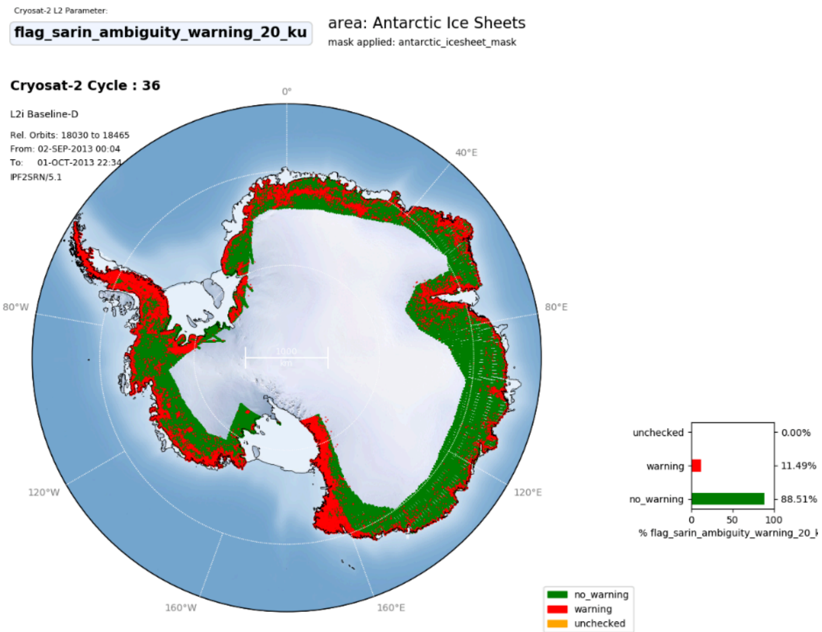

Figure 2.4: CryoSat-2 Phase Ambiguity Warning Flag

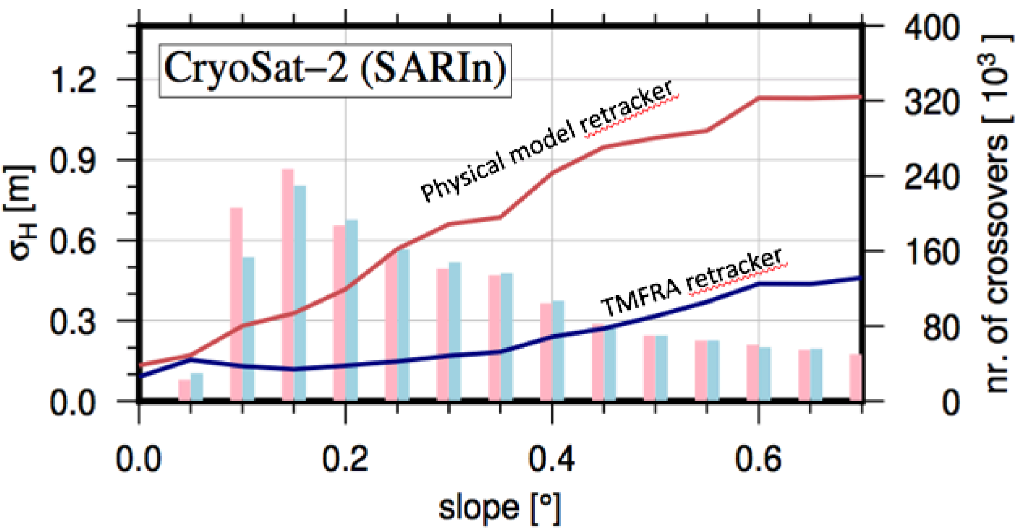

Figure 2.5: Precision of CryoSat-2 Measurements binned against slope (Schröder et al., (2019).

2.2.5 Data gaps and interpolation

For estimation of the ECV product at 5 or 10 km resolution, RA or LA measurements will leave many gaps (see Figure 2.6) due to the orbital pattern (especially for mission phases with a repeat cycle of ~30 days) and measurement failure (due to loss of track, low echo power, or complex waveforms that are difficult to retrack). The interpolation errors across these gaps will be determined by the covariance function of the satellite heights relative to a reference DEM, and the associated error covariance function of the grid values. To determine SEC from interpolated values at pixels away from repeated tracks is a challenge, and error estimates for this interpolation process will be based on repeat airborne laser validation data, where possible.. When estimated errors become excessive, no SEC ECV value will be produced. This will likely be the case for most ice sheet areas of surface slopes of more than 1° (as shown in Figure 2.3)

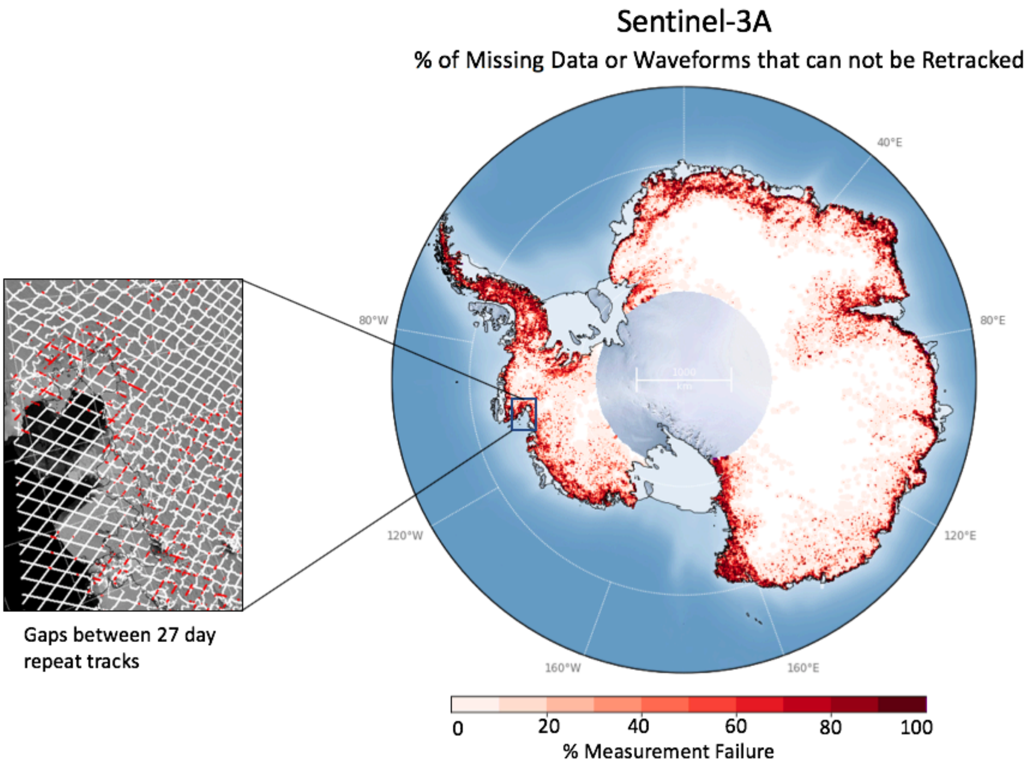

Figure 2.6: Typical Data Gaps and Measurement Failure for a 27-day Repeat Cycle of Sentinel-3A

2.2.6 Inter-satellite elevation bias

A full 33-year time series of elevations includes data from up to six RA missions and one LA mission, which must be co-registered to produce one continuous time series. Envisat is taken as the reference mission and its data is deemed to have no biases. Data from each other satellite is biased by a constant for that satellite over each grid cell. The biases between each temporally-overlapping pair of satellites are derived separately and combined later. For each overlapping pair of timeseries, the overlapping ends are modelled using least-squares regression to a seasonal cycle imposed on a linear gradient. The fitted model in each case is used to calculate elevation change in every month over a common two-year period, and the bias is taken as the median of the difference in the two elevation changes in this common period. This method can be adapted to calculate biases in areas larger than one pixel, e.g. by averaging all pixels in a drainage basin. The error due to the biasing is the root sum square of the 1-sigma uncertainties in the modelled differences between each overlapping pair.

2.3 Methodology for determination of error and uncertainty

Estimation of surface elevation errors are a propagation of errors of the individual measured RA/LA heights, including the estimated interpolation error from optimal estimation using the residual covariance functions, combined with the errors of the estimated geophysical corrections. However, because many of these errors are correlated between epochs, the error estimates of surface elevation cannot readily be converted to errors in surface elevation change. Therefore, SEC 5km dh/dt errors using the plane fit solution (McMillan, 2014) are calculated from the 1-sigma uncertainty of the SEC trend (Figure 2.7). Errors in elevation time series are calculated using the root mean square of the departure from the modelled trend.

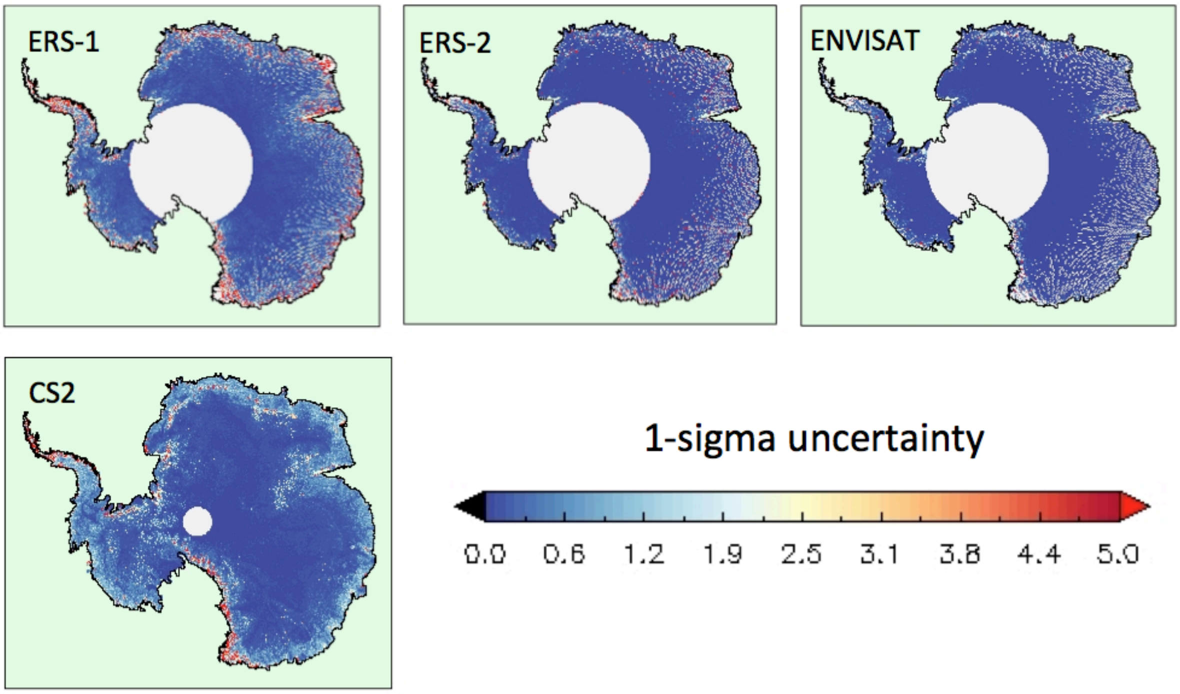

Figure 2.7: 1-sigma uncertainty of SEC dh/dt

Basin-wide elevation rate uncertainties are determined from the root sum square of the 1-sigma uncertainties, which are computed from all model solutions within each drainage basin, and from the biasing process. These uncertainties depend upon the distribution of elevation measurements accumulated within each grid cell and provide a measure of the extent to which our prescribed model of linear elevation change through time fits these observations. In consequence, they account for both departures from the prescribed model and for measurement errors which decorrelate within the sampling period, which is nominally 30 days. This statistical measure does not formally account for all sources of uncertainty, but will include factors such as radar speckle, errors in satellite location, retracker imprecision and unmodelled atmospheric attenuation (Wingham et al., 1998). When the spatial covariance of these error terms is assessed (Wingham et al., 1998), the variability is observed to decorrelate rapidly with increasing separation, in contrast to the covariance of the measured elevation rates themselves which remain relatively high. We interpret this to indicate that, at the scale of glaciological basins, these error terms alone do not adequately describe the certainty of estimates of mass imbalance. Specifically, the presence of signals, other than those of long-term imbalance, may introduce additional elevation rates over the observation period and must also be considered. These include snowfall variability and changes in snowpack characteristics.

ICESat and airborne laser data will be used as primary external data to evaluate the SEC, especially in the marginal zones and glacier systems where a long time history of airborne SEC is available. In the Antarctic CCI round robin experiment, the standard deviation of the differences between IceBridge and CCI Plane Fit SEC was 24.5cm/yr. Following the launch of ICESat-2, Operation IceBridge ended, resulting in no airborne laser altimetry observations being available to validate the CCI time-series after autumn 2019. Instead, SEC time-series of CryoSat-2 and ICESat-2 will be processed separately on the same 5 km by 5 km grid. The two time-series will be compared during the overlap period of the missions across the different drainage basins of Antarctica to assess the agreement between the independent satellite radar and laser altimetry datasets.

Further indications of systematic errors will come from comparisons of SEC across the different RA missions, ERS-1, ERS-2, Envisat, CryoSat-2, Sentinel-3A/3B and ICESat-2. The estimation of orbit biases between different methods will as a first approximation be done by comparison of ranges over marine areas, where mean sea level models combined with tidal models should in most cases be able to determine inter-mission orbit biases at the 10 cm level. It should be noted, however, that only spatially-invariant offsets mentioned in the footnotes to Table 2.1 can be found by comparison of ranges over marine areas. The inter-mission biases over land are spatially-variant, and improved estimation schemes have been discussed in Johannessen (2005) and Zwally (2005).

2.4 Error and uncertainty documentation

The overall errors in the SEC product will be a function of primarily the surface slope and the glaciological facies of the ice sheet regions (i.e., depending on bare ice, soaked, percolation or dry-snow zones). The overall accuracy of the products are difficult to quantify exactly prior to final ECV production phase, but error estimates across the ice sheet of 1-2 cm/yr seems realistic. This will, however, not apply to the ice sheet margin areas, where localized ice streams and glaciers will have much larger expected errors, or data be absent due to excessive surface slopes.

2.5 Guideline for using the product

The gridded ECV product for SEC in the Ice_Sheets_cci+ project will for the user provide both surface elevation change and estimated errors. The gridded representation of data will ensure that users have a product which is as close as possible for direct use, either as boundary/ground truth values for ice sheet modelling, media and outreach use, and – to some degree – for merging with other sensor change data (notably GRACE and other future ice change missions). Especially for joint estimations with GRACE the gridded representation of the ECV products mean that spatial averaging to recover SEC at a spectral resolution corresponding to GRACE is readily possible, even for non-specialists. The only drawback of the gridded representation at the given 5km resolution is the lack of resolution over narrow outlet glaciers, which typically show the largest changes.

2.6 References

Bamber, J.: Ice Sheet Altimeter Processing Scheme. Int. J. Remote Sensing, vol. 15, 925-938, 1994.

Brenner, A.C., R.A. Bindschadler, R.H. Thomas, H.J. Zwally: Slope-Induced Errors in Radar Altimetry Over Continental Ice Sheets, Journal of Geophysical Res., Vol. 88, 1983.

Faugere, Y, J Dorandeu, F Lefevre, N Picot and P Femenias: Envisat Ocean Altimetry Performance Assessment and Cross-calibration, Proceedings of the Montreux Envisat Symposium, 2007

Forsberg, R, L Sørensen, J Levinsen, J Nilsson: Mass loss of Greenland from from GRACE, CryoSat and ICESat. ESA CryoSat Symposium CD-proceedings, March 2013.

Johannessen O M, K Khvorostovsky, M Miles, L Bobylev: Recent Ice-Sheet Growth in the Interior of Greenland. Science, Vol. 310 no. 5750 pp. 1013-1016, doi: 10.1126/science.1115356, 2005.

Khvorostovsky K,: Merging and analysis of elevation time series over Greenland ice sheet from satellite radar altimetry. IEEE Trans. Geosc., Remote Sens., vol., 50, 1, pp. 23-36, 2012.

Lacroix P., B. Legrésy, F. Rémy, F. Blarel, G. Picard, and L. Brucker, :Rapid change of snow surface properties at Vostok, East Antarctica, revealed by altimetry and radiometry, Remote Sens. Environ., vol. 133, no. 12, pp. 2633–2641, 2009.

Markus, T., Neumann, T., Martino, A., Abdalati, W., Brunt, K., Csatho, B., et al. (2017). The ice, cloud, and land elevation satellite-2 (ICESat-2): Science requirements, concept, and implementation. Remote Sensing of Environment, 190, 260–273.

McMillan M., Muir A., Shepherd A.,Escola R.,Roca M.,Aublanc J, Thibaut P., Restano M.,Ambrozio A.,Beneviste J. : Sentinel-3 Delay-Doppler altimetry over Antarctica, Cryosphere 2019.

Jan Wuite, et al., End-to-end Uncertainty Budget (E3UB) for the Antarctic_Ice_Sheet_cci+ project of ESA's Climate Change Initiative, version 1.0 (2015).

Schutz B. E., H. J. Zwally, C. A. Shuman, D. Hancock, and J. P. DiMarzio: Overview of the ICESat Mission. GRL, VOL. 32, L21S01, doi:10.1029/2005GL024009, 2005

Shepherd, A. and Wingham, D.: Recent sea-level contributions of the Antarctic and Greenland ice sheets: Science, v. 315, p. 1529-1532, 2007.

Shepherd, A. et al., Algorithm Theoretical Basis Document (ATBD) for the Antarctic Ice Sheet CCI project of ESA's Climate Change Initiative, version 2.1 (2017).

Schröder, L., Horwath, M., Dietrich, R., Helm, V., Van Den Broeke, M. R., & Ligtenberg, S. R. (2019). Four decades of Antarctic surface elevation changes from multi-mission satellite altimetry. The Cryosphere, 13(2), 427-449.

Sørensen, L.S., Simonsen, S.B., Nielsen, K., Lucas-Picher, P., Spada, G., Adalgeirsdottir, G., Forsberg, R., and Hvidberg, C.S.: Mass balance of the Greenland ice sheet (2003-2008) from ICESat data - the impact of interpolation, sampling and firn density. Cryosphere, v. 5, p. 173-186, 2011.

Studinger, M., Smith, B. E., Kurtz, N., Petty, A., Sutterley, T., & Tilling, R. (2023). Estimating differential penetration of green (532 nm) laser light over sea ice with NASA's airborne topographic mapper: Observations and models. The Cryosphere, 18, 2625–2652. https://doi.org/10. 5194/tc-2023-126

Wingham D J, A Shepherd, A Muir, G.J Marshall: Mass balance of the Antarctic ice sheet. Phil. Trans. R. Soc vol. 364 no. 1844 1627-1635, doi: 10.1098/rsta.2006.1792, 2006.

Vignudelli, S, A. G. Kostianoy, P. Cipollini, J. Benveniste (editors): Coastal Altimetry, Springer-Verlag, doi:10.1007/978-3-642-12769-0, 2011.

Zwally, H J, M B Giovinetto, J Li, H G Cornejo, M A Beckley, A C Brenner,Jack L. Saba, Donghui Y: Mass changes of the Greenland and Antarctic ice sheets and shelves and contributions to sea-level rise: 1992–2002. Journal of Glaciology, Vol. 51, No. 175, 2005.

3 Ice Velocity and Ice Velocity Change

3.1 Introduction

In Phase 2 of the project, development efforts are focussed on integrating SAOCOM SAR data into the processing chain and testing InSAR-augmented ice velocity (IV) retrieval for Antarctica, following the approach previously applied in the Greenland Ice Sheet CCI. The existing InSAR and offset tracking (OT) processing pipelines, originally developed for other sensors in previous CCI phases, have been adapted to support SAOCOM data as well as combined SAOCOM and Sentinel-1 processing. Sources of errors and uncertainties in the ice velocity processing chain—both internal (algorithm-dependent) and external—along with accuracy assessment methods, were extensively discussed in [RD1] and [RD2]. These are updated here with a specific focus on SAOCOM and InSAR.

Additionally, in this phase of the project preparations are made for a new Essential Climate Variable (ECV) product on Ice Velocity Change (IVC). The IVC processing chain, currently under development, is described in [RD3]. The IVC product will provide the spatial distribution of ice flow rate changes over defined time intervals, derived from existing IV maps. The primary sources of uncertainty and error remain the same as in IV processing (offset tracking), with the overall error in the IVC product calculated as the root sum square of the uncertainties associated with the velocity maps used for differencing.

3.2 Sources of error

3.2.1 Baseline errors

Errors in the annotated state vectors of the input SAR SLC images lead to inaccuracies in baseline calculations, resulting in residual phase contributions in the interferogram. This issue is more pronounced for SAOCOM compared to Sentinel-1 due to SAOCOM's lower-quality orbits. Interferometric applications require precise orbit control, including accurate pointing and synchronization between interferometric pairs. Sentinel-1's precise orbits, typically available 21 days after acquisition, have a nominal accuracy of 5 cm (3D RMS). For interferometry, the key factor is the relative orbit error (baseline error) projected onto the line-of-sight direction, as it directly impacts the ice velocity measurements. Since orbital errors are generally low-frequency, they can largely be corrected through low-order polynomial calibration of the interferometric displacement measurement. This calibration method is detailed in (RD3) and Mohr & Boncori (2008).

3.2.2 Coregistration errors

The major challenge in employing interferometry on Sentinel-1 TOPS data over ice sheets is the azimuth-dependent squint angle inherent in the beam steering employed in the Interferometric Wide (IW) swath mode. An azimuth shift, Δx, not accounted for in the coregistration will lead to a phase shift, Δϕ (De Zan et al., 2014):

$$\Delta\phi=4\pi/\lambda\ \Delta x \square \sin \sin \beta$$

where λ is the radar wavelength and β is the squint angle (the angle off broadside at which the target is in the centre of the antenna beam). The azimuth shift can arise both from global coregistration errors (i.e. orbital errors), from ionospheric artefacts, or from actual horizontal azimuth motion associated with the ice flow between the two acquisitions. The phase sensitivity to azimuth shift is much smaller than for shifts in the range direction, since the variation of β along a burst is on the order of ±1°. At burst boundaries, however, the squint angle changes abruptly, which can cause problems for the phase unwrapping, leading to burst-to-burst discontinuities. The azimuth shift necessary to produce a phase jump of π across a burst boundary with squint angle +β and -β at the two burst edges is:

$$\Delta x=\lambda/(\beta\ )$$

which for typical values of β=1° for Sentinel-1 is 0.4m. Orbital errors for S1 will typically not be of this magnitude but could be observed for ionosphere-induced azimuth shifts. For real ice flow in the azimuth direction, this corresponds to an ice velocity of just 7 cm/day (25 m/y), assuming a 6-day temporal baseline. Employing an external ice velocity map derived from a multi-year average of offset-tracking measurements (or other sources), the bulk of the azimuth motion can be compensated for, as described in (RD3). Because SAOCOM has a much larger orbital tube and generally no burst synchronisation in TOPSAR mode we use SAOCOM StripMap (SM) data. Therefore, in contrast to Sentinel-1 TOPS, phase jumps are not a concern.

3.2.3 Decorrelation

The interferometric phase quality is affected by various contributions, and is measured by the interferometric coherence, which is a number between 0 and 1. The contribution of the different decorrelation effects on the coherence can be summed up by Scheiber et al. (2000):

$$\gamma=\gamma_{SNR}\cdot\gamma_{spatial}\cdot\gamma_{misreg}\cdot\gamma_{temporal}$$

At the frequency of Sentinel-1, the ice generally has a high backscatter (and hence SNR), so that the decorrelation due to thermal noise, γSNR, is small. Spatial decorrelation is also limited in Sentinel-1 data due to the small orbital tube. Since an ice sheet presents a non-stationary scenario, misregistration can occur due to ice motion between acquisitions, even if the sub-resolution structure remains stable. The impact on the coherence of a range or azimuth misregistration, Δ, is given by:

$$\gamma_{misreg}=\Delta/\rho \;, \quad |\delta|<\rho$$

where ρ is the resolution in the relevant dimension, and sinc(x)=sin(πx)/(πx). For a misregistration larger than one resolution cell, the coherence drops to zero. Sentinel-1 has the highest resolution in the range direction of approximately 2.5 m, which means that for a 6-day interferogram, an ice flow velocity projected in the range direction of 2.5 m/6 days = 0.44 m/d (160 m/y) leads to complete decorrelation if not accounted for. The use of a multi-year averaged external ice velocity map derived from offset-tracking (see (RD3)) in the coregistration procedure can account for the bulk of this effect.

SAOCOM operates at L-Band which covers areas decorrelating in C-band, being less affected by decorrelation in areas with strong velocity gradients due to reduced fringe frequency enabling reliable phase unwrapping. On the other hand, the L-band is more sensitive to disturbances by ionospheric effects, which need to be corrected.

Finally, temporal decorrelation occurs when the scene scattering properties change between image acquisitions, for example due to melt, snowfall or ice dynamics, and is the major contributor to coherence loss in IV estimation. The repeat-pass period for the Sentinel-1 mission is since decommissioning of S1B 12 days; for SAOCOM this is 16 days for one satellite, but 8 days for the constellation.

A low coherence leads to noise on the phase estimate, which again leads to noise on the displacement estimate. The phase variance associated with a given coherence level is given by Rodriguez and Martin (1992):

$$\sigma_\varphi^2=\frac{1}{2N_L}\,\frac{1-\gamma^2}{\gamma}$$

3.2.4 GCP uncertainty

Interferometric displacement is a relative measurement, as the unwrapped phase is referenced to an initial point where the phase is only known modulo 2π. Additionally, it is influenced by orbit errors and TOPS coregistration effects, as discussed in Sections 3.2.1 and 3.2.2. Any bias in the phase unwrapping reference point will propagate across the entire image, necessitating calibration using ground control points (GCPs) with known displacement. In ice sheet scenarios, identifying non-moving, phase-connected bedrock points can often be challenging. When such stable reference points are unavailable, moving GCPs must be used instead. As outlined in [RD3], we utilize GCPs in slow-moving regions, preferably along ice divides, as these areas typically exhibit minimal variation. However, uncertainties in GCP velocity will impact the calibration and must be accounted for, as detailed in Section 3.3.

3.2.5 Phase unwrapping errors

Phase unwrapping errors can occur due to steep phase gradients in the interferograms, phase discontinuities at burst or swath boundaries caused by azimuth misregistration (see Section 3.2.2), or disconnected phase regions within the image. The unwrapping process utilizes a minimum cost flow (MCF) algorithm, where coherence values and intensity edge detection are used to generate weighting factors. The MCF algorithm can to some extent exploit the reduced coherence at burst boundaries to unwrap “around” these discontinuities.

A segmentation mask indicating disconnected segments in the unwrapped phase field is generated and output, and absolute phase estimation is first carried out on a main segment (by default the largest segment from the unwrapping segmentation mask), by averaging the difference of the calculated and measured path lengths to each of the GCP’s in this segment having a valid interferometric phase. Absolute phases are then estimated for each of the remaining segments. Segments without valid GCP’s are discarded. If the segmentation process is incorrect, it can introduce unwrapping errors within misconnected regions. To address this, an error prediction module attempts to model and account for these errors, as described in Section 3.3.

3.2.6 Velocity inversion errors

Since interferometry measures displacement only in the radar line-of-sight direction, obtaining horizontal velocity estimates requires imaging each point from multiple viewing directions—specifically, from both ascending and descending tracks (e.g., SAOCOM-SAOCOM or SAOCOM-Sentinel-1) covering the same region. At high latitudes, these tracks are nearly orthogonal, allowing for better velocity resolution. However, at lower latitudes, the crossing angle decreases, leading to poor resolution in the North-South direction, as both line-of-sight vectors are predominantly aligned in the East-West direction. By incorporating uncertainty estimates for each line-of-sight observation, the resulting errors in the 2D velocity field can be quantified as part of the velocity inversion process.

If only a single line-of-sight (LOS) velocity map is available or if there are gaps in the interferometrically derived ice velocity from one LOS direction, interferometric velocity measurements can be combined with offset-tracking-derived flow directions. These flow directions are typically obtained from a multi-annual offset-tracking velocity map (when available). While they introduce some additional uncertainty, this is generally considered minimal.

3.3 Methodology for determination of error and uncertainty

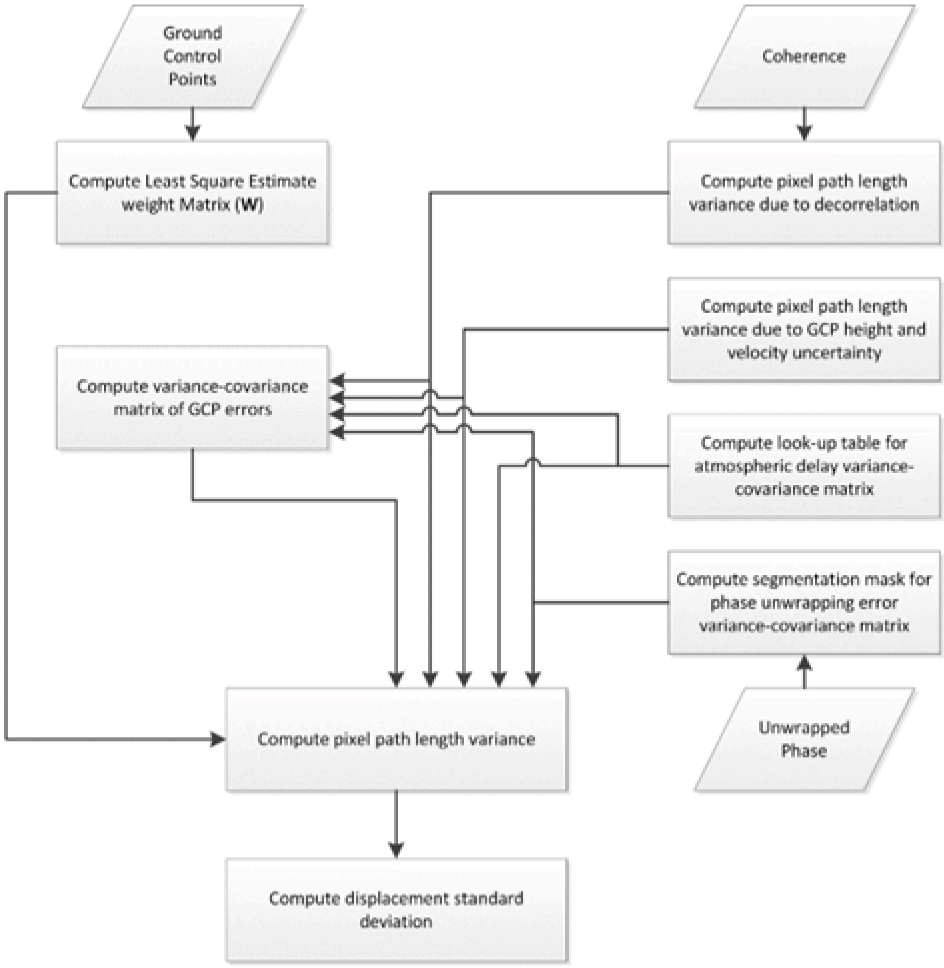

Figure 3.1: Error prediction framework for interferometric displacement measurement.

Error prediction is based on a mathematical framework for baseline error calibration, described in detail in Mohr and Boncori (2008) and Boncori and Mohr (2008). Estimation of the baseline errors is modelled as a least square problem in the presence of correlated noise. The error sources considered are interferometric decorrelation, GCP height and velocity uncertainty, atmospheric propagation and phase unwrapping. Phase unwrapping errors between any two pixels within the unwrapped phase field are considered to be a zero-mean random variable and an attempt is made to model their covariance. This is done in two steps. A segmentation mask is derived at first, based on the residue density and jumps greater than π radians in the unwrapped phase file, and subsequently this is used to assign the error covariance between pixel pairs. The segmentation mask serves the purposes of identifying consistently unwrapped regions.

As shown in Figure 3.1, statistical models for each of the main error sources are used to compute a variance-covariance matrix of the electrical path-length errors affecting the GCPs used for baseline refinement. Together with the weight matrix used during interferometric processing for baseline estimation, this allows computation of the error variance of each calibrated pixel path-length. Path-length error variances are finally converted to height and displacement error standard deviations. These estimates are propagated in the velocity inversion to errors on Easting and Northing velocities when combining line-of-sight measurements from crossing tracks. In areas where multiple tracks are combined, the error estimates are used to do a weighted average of the displacement measurements, and the error estimate of the output product is updated to reflect this.

3.4 Error and uncertainty documentation

The output from the error prediction described in the previous section is a pixel wise estimate of the standard deviation and is provided with the IV product.

3.5 Guideline for using the product

The IV and IVS products are distributed as NetCDF or GeoTiff files following the conventions described in the Antarctic_Ice_Sheet_cci Product User Guide (PUG)(RD3). The estimated error standard deviations are included and are provided in the same grid as the ice velocity estimates.

3.6 Uplift from InSAR line-of-sight velocity

The uplift prototype product does not, for now, come with an associated error estimate. The primary use of the product is detecting transient uplift events indicating subglacial water transport, which does not require an error estimate in itself but rather an understanding of what uplift patterns look like. When events have been detected, the amount of uplift/subsidence (over the InSAR temporal baseline period) can be estimated, but this requires careful analysis, as the error sources are not easily quantified must be accounted for, and the signals from subsidence can be very small compared to the typical displacements due to horizontal ice flow. The following errors can affect the estimate:

1) Unwrapping errors occur when the interferometric phase unwrapping adds an incorrect number of phase cycles to the interferometric phase across a region in the image. These errors typically result in unphysical, sharply delineated regions of bias compared to the surroundings, and no measurements in such regions should be trusted. An example is shown in Figure 3.2.

2) Atmospheric artifacts can arise from both ionospheric scintillations, and from variations in the tropospheric water content affecting the radar signal propagation. They are typically correlated on a much larger spatial scale than the localized uplift/subsidence signals. Sometimes, the atmospheric signal arises from propagation conditions in a single image, and when this image is used in two subsequent InSAR pairs (i.e., as the first image in one interferogram and as the last image in the subsequent interferogram), the atmospheric signal reverses sign between the two resulting displacement maps.

3) All DInSAR measurements are calibrated using ground control points (GCPs) of assumed known velocity. This is done for each displacement map by fitting a plane to the observed velocity differences (measured minus known GCP velocity) and subtracting the plane fit from the displacement map. GCPs are placed across the image in slow-moving regions, i.e. outside of ice streams and glaciers, where the velocity variations are assumed negligible. Atmospheric propagation variations can, however, due to their large spatial correlation, introduce errors at many GCPs, resulting in calibration errors. These kinds of errors exhibit a bilinear variation across the image, i.e. a "tilt" of the displacement map. An example of this is shown also in Figure 3.3, which exhibits a linear tilt from top left to bottom right.

4) Horizontal flow changes. Although the uplift estimate provided in this product is generated by assuming negligible horizontal flow changes, such changes do occur, especially in faster flowing regions like ice streams and glaciers.

If trying to quantify observed uplift/subsidence events, the biases introduced by the error sources described above should be accounted for, e.g. by estimating the bias in a region surrounding the uplift event.

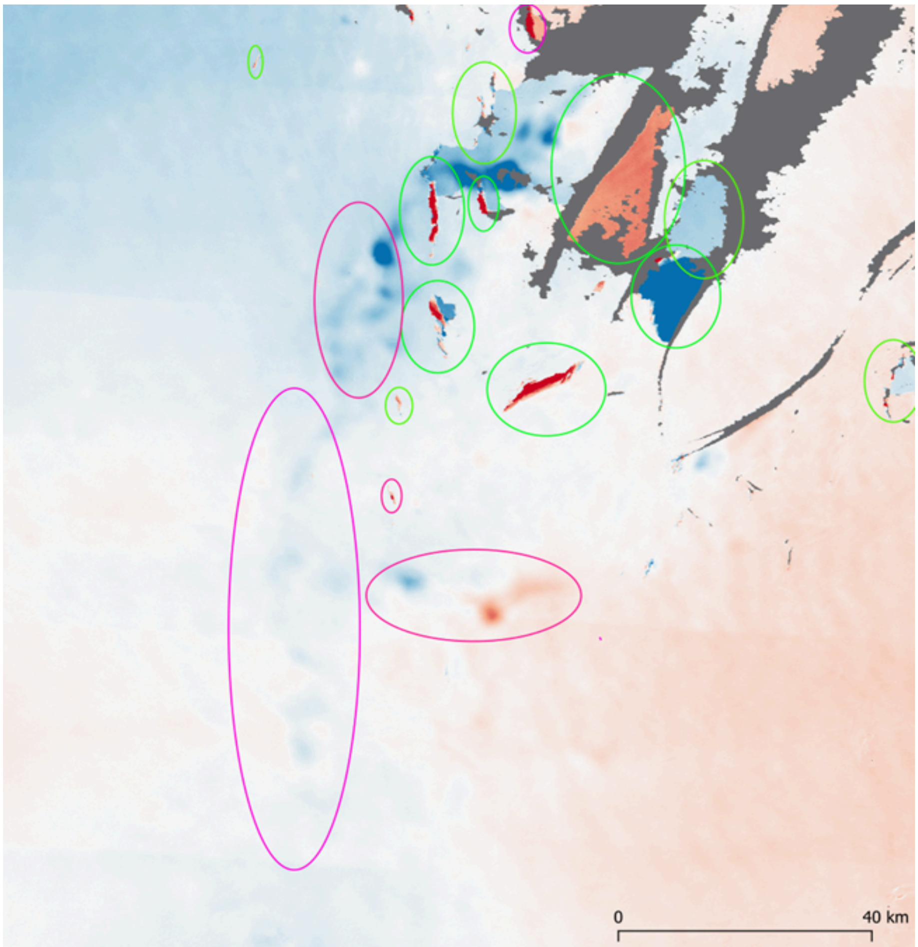

Figure 3.2: Examples of unwrapping errors and real uplift/subsidence signals from Greenland. The areas in the magenta ellipses represent real geophysical signals, whereas areas in green ellipses contain phase unwrapping artifacts, characterized by a sharp delineation to the surroundings.. The linear gradient from the top-left to the bottom right corner is typically the result of a calibration error, and likely not caused by surface displacement.

3.7 References

Mohr, J.J.; Boncori, J.P.M.: An Error Prediction Framework for interferometric SAR Data. IEEE Transactions on Geoscience and Remote Sensing (2008), Vol 46, pp. 1600-1613.

De Zan, F; Prats-Iraola P.; Scheiber, R.; Rucci,A..: Interferometry with TOPS: coregistration and azimuth shifts, Proceedings of EUSAR 2014, June 2014, pp. 949-952.

Scheiber, R.; Moreira, A.: Coregistration of interferometric SAR images using spectral diversity, IEEE Transactions on Geoscience and Remote Sensing (2000), Vol 38, no. 51, pp. 2179 –2191.

Rodriguez, E.; Martin, J.M.: Theory and design of interferometric synthetic aperture radars, IEE Proceedings-F(1992), Vol 139, no. 2, pp.147-159.

Boncori, J.P.M. and Mohr, J.J.: A tuneable closed form model for the structure function of tropospheric delay. IEEE Geoscience and Remote Sensing Letters (2008) , Vol. 5, pp. 222-226.

4 Grounding Line Location and Grounding Line Migration

4.1 Introduction

A theoretical error characterisation is important for the GLL since the availability of ground-based measurements, which would allow for an end-to-end validation, parallel to the satellite acquisitions is extremely rare. The error and uncertainty characterisation of the GLL is strongly dependent on the delineation method used. In the AIS_cci phase 2016 – 2018 and AIS_cci+ phase 1 this was carried out manually. Although the automatization of the process was tackled in the various stages of the project, none of the two initially proposed methods we considered. Neither the gradient threshold classification nor the fringe frequency, was deemed appropriate to be implemented in the operational environment. So the digitalization of the upper limit of the ice flexure indicated by the dense InSAR fringe belt remained manual and revealed large systematic uncertainties. The digitization error is bigger than all other error sources in earlier product generation steps. In order to address this problem, in the current phase 2 of AIS_cci+ a machine learning based delineation method is foreseen to be implemented [AD3].

For the new Grounding Line Migration product the error assessment will be provided in the AIS_cci+ phase 2 optional activity "Grounding Line Migration (GLM) - A New Parameter for the Antarctic Ice Sheet".

4.2 Sources of error

The error sources are separated into two parts – the required InSAR processing which generates the basis for the GL derivation and the actual process of GL delineation itself. The error sources in the InSAR processing are mainly phase filtering and geolocation errors due to orbit and DEM uncertainties as well as uncorrected tropospheric and ionospheric delays.

For the GLL derivation the error sources depend on the method used for delineation. For the manual delineation process the average values resulted from the Round Robin performed in AIS_cci 2016 - 2018 are considered unchanged and provided again in this document. The error coming from the machine learning - based delineation method is quantified from current experiments.

4.3 Methodology for determination of error and uncertainty

A common approach to validate results and evaluate errors and uncertainties is the comparison against external data. For the GLL this step is difficult since the GLL location shifts with a varying sea level due to ocean tides. This shift can easily rise up to 5 km which is far beyond the requested accuracy.

For the current grounding line processing, the used DEM has been updated to the Copernicus 90m DEM. In order to estimate the impact of the DEM height errors on the horizontal location of the considered point, an approximation is done based on typical values found in the error map of the DEM. Resulting positioning errors can be found in Table 4.1.

For the newly implemented GL delineation model the predictive uncertainty is estimated by training an ensemble of five neural networks. Similar to the Round Robin exercise carried out in AIS_cci the concept of an ensemble consists of repeating GL delineation for each sample with multiple networks. A different random seed was set for each network, which initialized them with a different set of random weights and a shuffled order of training samples (Lakshminarayanan et al., 2017). Figure 4.1 shows an example of pixel-wise mean and standard deviation of predicted probabilities for each sample resulting from the five neural network ensembles. The mean probabilities are converted to mean GLs through a sequence of binarisation, filtering and skeletonisation operations.

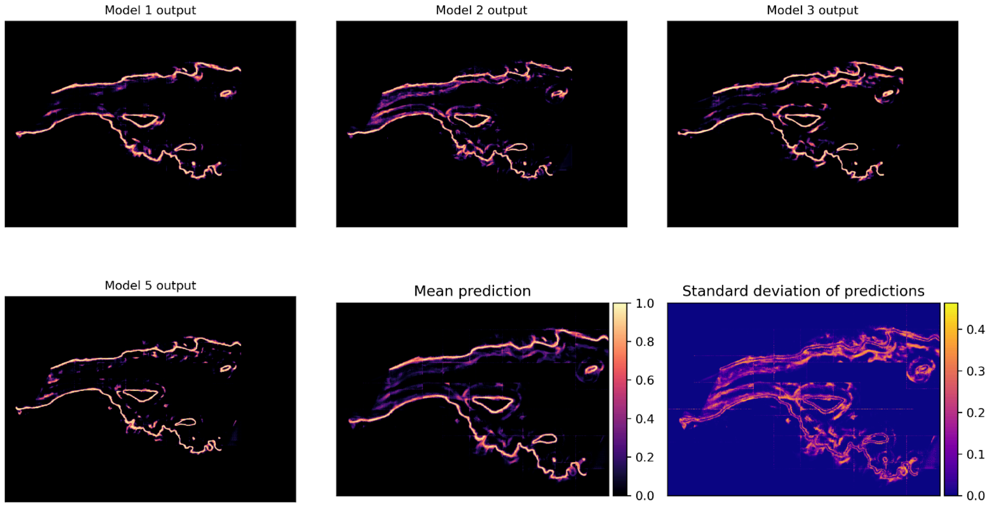

Fig. 4.1: Mean and standard deviation of an ensemble of five predictions over Amery ice shelf.

4.4 Error and uncertainty documentation

4.4.1 InSAR processing uncertainties

In standard interferometric applications like e.g. when single phase measurements of the interferogram are utilized, the InSAR error characteristic is related to the operations applied during the InSAR processing. This includes for example image-to-image co-registration, resampling method, and phase filtering which all affect the phase values. This is also true in the present GL detection procedure, but the phase values themselves are no “measurements” in our case. They portray a shape which will be extracted and this simplifies the situation. There are two major error sources in InSAR processing which are relevant to our application:

1) Effect of phase filtering on the shape of the GL

2) The absolute geolocation accuracy after geocoding

During the InSAR processing, phase filtering is applied to noisy double difference interferograms in order to suppress the phase noise which consequently enhances the quality of the fringe belt for the machine learning approach. The filtering process utilizes the Goldstein phase filter. A test was performed in order to confirm that the phase filtering does not bias the GLL. Figure 4.2 shows the filtered vs. the unfiltered phase and there is no evidence that locations would be shifted due to filtering.

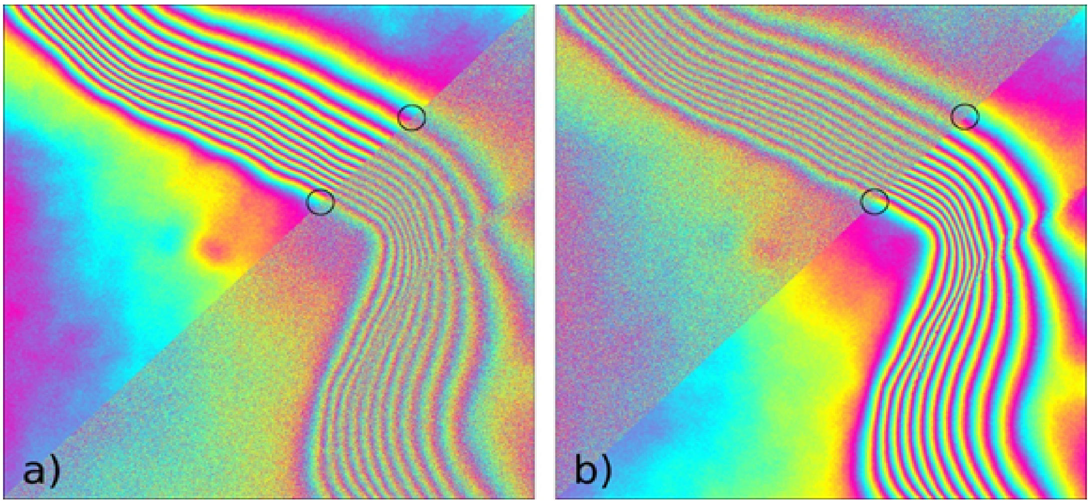

Fig. 4.2: The effect of the Goldstein filter applied to a double difference interferogram. For visualization and comparison the filtered image was split into two triangles and plotted as (a) and (b) over the original phase image. As one would expect from such a filter, there is no evidence that the solution is biased. The location of the GL feature marked as black circles is consequently not affected.

The absolute geolocation accuracy depends on the used orbit products, ionospheric and tropospheric delays and most importantly on the accuracy of the DEM. The accuracy of precise TerraSAR-X and Sentinel-1 orbit products are smaller than 20 cm (Breit 2010, ESA 2014). For ERS, DEOS orbits are used which have an accuracy of ±15 cm. Uncorrected ionospheric delays can cause ~1 dm in X-Band and ~4 dm in C-Band while the tropospheric delays are frequency independent and in the order of 2 m to 4 m. The biggest error source however is the accuracy of the used DEM.

Since the previous AIS_cci 2016-2018 phase of the project new adequate continental-wide DEMs were released and replaced the older DEMs in the interferometric part of the GLL processing chain. We are using the Copernicus DEM - Global and European Digital Elevation Model which is an edited version of the TanDEM-X global DEM available in 3 different resolutions. The absolute horizontal position errors of different DEMs in difficult terrain conditions of Copernicus DEM in respect to the historical DEMs used previously in the project are given in Table 4.1. The absolute horizontal and vertical accuracies of TanDEM-X and Copernicus DEMs are below 10 m, while the relative vertical accuracy is < 2m (slope < 20°) and < 4m (slope ≥ 20^0). The availability of high resolution DEMs is crucial to obtain an undistorted dense fringe belt in the GZ which contributes to an accurate derivation of GLL.

Table 4.1: Horizontal position accuracies of different DEMs in Antarctica. *Since the effect of the DEM is a systematic error it would reduce in the differential case if equal orbit geometries were used for the re-observation.

DEM	Maximum height error [m]	*Absolute horizontal position error [m] at incidence angle		
		30°	40°	50°
Bamber (Bamber, 2009)	70	121.24	83.42	58.73
Bedmap2 (Fretwell, 2013)	130	225.16	154.92	109.08
TanDEM-X/Copernicus DEM	10	17.32	11.91	8.39

4.4.2 GL deviation uncertainties

If manual GL delineation will be applied, uncertainty measurements derived from the Round Robin (RR) experiment will be assumed. They purely account for digitizing errors, possible systematic errors as described before would add to the error budget. The four categories defined for this purpose are shown in Table 4.2.

Table 4.2: Quality Categories for manual delineation based on obtained Round Robin results.

Category	Description	Average error
1	good coherence, simple and clear features	~ 200 m
2	good coherence, complicated features mixed with remaining topographic effects	~ 800 m … 1.2 km
3	bad coherence, simple and clear features	~ 1.2 km … 1.5 km
4	bad coherence, complicated features	~ > 1.5 km

In order to assess the uncertainty of the machine learning based delineations, the network ensemble predictions detailed in Section 4.3 are used. The distance is measured between the average grounding line and the nearest boundary of the uncertainty polygons every ten kilometres of the mean GLs. Their average is computed to form an aggregate standard deviation for the entire test set. Table 4.3 shows the metrics and average standard deviation of ensembles of two networks trained with different feature subsets. Details of the methodology can be found in [Ramanath et al, 2024]. Summarizing the results we state that the ensemble GLs have a median deviation of 222 m and a mean deviation of 341 ± 374 m from the AIS_cci GLLs. This is in the same order as the average error in case of manual delineations of best quality fringes (Category 1 in Table 4.2).

Table 4.3: Performance of ensemble networks described in Section 4.3. The metrics are calculated for the ensemble average GLs. The uncertainty measure is 1 standard deviation and is computed as the average of one-way distances from the average GLs to the nearest uncertainty buffer contour.

Features subset	Median distance [m]	Mean distance [m]	MAD [m]	Mean coverage [%]	ODS F1 score	Average precision
Rectangular components +non-interferometric	222	341 ± 374	109	69	0.2	0.13
Rectangular components	265	421 ± 402	141	65	0.16	0.11

4.5 Guideline for using the product

Since our error estimations are static values there is no annotation of the error in the GLL product itself. No other datasets (e.g. MEaSUREs GLL) have such information we will recommend to the user to consult the publicly available documentation of the project.

4.6 References

Bamber, J. L., Gomez-Dans, J. L. und Griggs, J. A. (2009). A new 1 km digital elevation model of the Antarctic derived from combined satellite radar and laser data. Part 1: Data and methods. The Cryosphere, 3(2):101–111.

Breit, H. and Fritz, T and Balss, U. and Lachaise, M. and Niedermeier, A. and Vonavka, M. (2010) TerraSAR-X SAR Processing and Products, IEEE Transactions on Geoscience and Remote Sensing, Volume: 48, Issue: 2, pp: 727-740, DOI:10.1109/TGRS.2009.2035497

Fretwell, P., Pritchard, H. D., Vaughan, D. G., Bamber, J. L., Barrand, N. E., Bell, R., Bianchi, C., Bingham, R. G., Blankenship, D. D., Casassa, G., Catania, G., Callens, D., Conway, H., Cook, A. J., Corr, H. F. J., Damaske, D., Damm, V., Ferraccioli, F., Forsberg, R., Fujita, S., Gim, Y., Gogineni, P., Griggs, J. A., Hindmarsh, R. C. A., Holmlund, P., Holt, J. W., Jacobel, R. W., Jenkins, A., Jokat, W., Jordan, T., King, E. C., Kohler, J., Krabill, W., Riger-Kusk, M., Langley, K. A., Leitchenkov, G., Leuschen, C., Luyendyk, B. P., Matsuoka, K., Mouginot, J., Nitsche, F. O., Nogi, Y., Nost, O. A., Popov, S. V., Rignot, E., Rippin, D. M., Rivera, A., Roberts, J., Ross, N., Siegert, M. J., Smith, A. M., Steinhage, D., Studinger, M., Sun, B., Tinto, B. K., Welch, B. C., Wilson, D., Young, D. A., Xiangbin, C., and Zirizzotti, A.: Bedmap2: improved ice bed, surface and thickness datasets for Antarctica, The Cryosphere, 7, 375–393, https://doi.org/10.5194/tc-7-375-2013, 2013.

Lakshminarayanan, B., Pritzel, A., and Blundell, C. (2017). Simple and Scalable Predictive Uncertainty Estimation using Deep Ensembles, in: Advances in Neural Information Processing Systems, edited by Guyon, I., Luxburg, U. V., Bengio, S., Wallach, H., Fergus, R., Vishwanathan, S., and Garnett, R., vol. 30, Curran Associates, Inc., https://proceedings.neurips.cc/paper_files/paper/2017/file/9ef2ed4b7fd2c810847ffa5fa85bce38-Paper.pdf

Ramanath Tarekere, S., Krieger, L., Floricioiu, D., and Heidler, K.: Deep learning based automatic grounding line delineation in DInSAR interferograms, EGUsphere [preprint], https://doi.org/10.5194/egusphere-2024-223, 2024.

5 Gravimetric Mass Balance

5.1 Introduction

Errors in GRACE-derived mass change estimates from GRACE and GRACE-FO (both referred to as GRACE in the following)s have several origins. The three major contributions arise from:

1. GRACE errors in the monthly gravity field solutions.
2. Leakage errors due to the limited spatial resolution achieved by GRACE.
3. Errors in models used to reduce superimposed mass signals.

In the following we will give an overview on the different sources of errors, the applied methodologies for their assessment and a description of the accuracy measures provided along with the GMB products. More detailed discussions on selected aspects have been given previously have been given by, e.g., by Wahr et al. (2006),; Horwath and Dietrich, (2009);, Velicogna and Wahr, (2013);, Barletta et al. (2013), Blazquez et al. (2018), Groh et al. (2019) and more studies cited in what follows.

A more detailed description of the uncertainty characterisation approach and results for the AIS_cci GMB products is given by Groh and Horwath (2021).

5.2 Sources of error

5.2.1 Noise in monthly gravity field solutions

Monthly GRACE solutions (usually represented by a set of spherical harmonic Stokes coefficients) are significantly afflicted by errors. The errors have a pronounced covariance structure, induced by the different sensitivities of the GRACE observations to different parts of the spherical harmonic spectrum and by the different susceptibility of parts of the spectrum to modelling errors involved in the GRACE processing procedure.

In geographic representations of gravity field, or mass, changes from GRACE, the typical north-south striping is a representation of the GRACE error covariance structure. One reason is the along-track (hence mainly north-south) direction of the ranging observations between the twin satellites, giving higher sensitivity to these directions (e.g. Schrama et al. 2007). A second reason arises from temporal gravity field changes within a month. Satellite tracks that are distant in time may be close (and approximately parallel) in space. Therefore, the actual temporal variations may alias into striping patterns of spatial variations (Wiehl and Dietrich 2005, Seo et al. 2008). GRACE processing involves de-aliasing procedure, where high-frequency tidal and non-tidal mass variations in atmosphere and ocean are reduced from the observations using Atmosphere and Ocean De-aliasing Level-1B (AOD1B) products (Flechtner et al., 2015). Nevertheless, limitations in the utilised background models will lead to aliasing in GRACE monthly solutions caused by residual mass variations which have not been reduced. Processing centres provide calibrated errors, derived by a degree-dependent scaling of formal errors for each coefficient, as an estimate for the correlated GRACE errors.

Algorithms for the determination of mass changes intend to minimise GRACE error effects, e.g. by means of a suitable filter. Since available approaches are not able to entirely remove correlated errors, residual errors will be inevitably propagated to regional mass change estimates.

5.2.2 Signal leakage

The limited spatial resolution of GRACE, caused by the attenuation of small-scale gravity changes at satellite altitude, induces signal leakage. Signals from adjacent regions cannot be precisely separated. In this way, signals from outside a region (e.g. a drainage basin) may leak into the regional estimate (leakage-in). Likewise, mass signals within the region under investigation may not be completely recovered, but under- or overestimated (leakage-out). Leakage errors are most pronounced for the investigation of small regions. Since leakage errors are related to actual mass changes, they are not uncorrelated from month to month. Their temporal correlation behaviour is instead inherited from the respective behaviour of the underlying mass changes.

Leakage-out originates from mass changes of the AIS itself. Variations in SMB cause leakage on inter-annual and long-term scales. Changes in ice dynamics, i.e. ice discharge, induce leakage mainly affecting long-term signal components (e.g. linear trends). Mass changes causing leakage-in may be subdivided into near-field and far-field signals. Ice mass changes in neighbouring drainage basins are one distinct source of leakage-in. Moreover, mass variations of the surrounding ocean, in particular due to variations of the Antarctic Circumpolar Current (ACC), are difficult to isolate from near coastal ice mass change. They are therefore another potential origin of leakage-in. Since oceanic mass variations have been largely removed during the GRACE de-aliasing process using AOD1B products, only residual variations, due to the incompleteness of the utilised background models, will possibly bias the ice mass estimates. The same applies to high-frequency mass changes of the atmosphere. Leakage from far-field regions stems from continental hydrology, oceans and globally distributed ice masses such as the GIS, glaciers, and ice caps.

5.2.3 GIA

Vertically superimposed mass redistributions cannot be separated from GRACE gravity observations alone. This fact particularly concerns the superposition of present-day ice mass changes and GIA. Geophysical models of GIA may be employed to resolve this ambiguity. GIA-induced mass changes can be assumed to be linear over observational periods of satellite missions. Model predictions of present-day linear trends in GIA are used to reduce monthly GRACE solutions.

Beside a model describing the visco-elastic properties of the Earth, GIA models require a reconstruction of glacial history based on glaciological or geomorphological evidence on former ice extent and indicators of past sea level. Since these evidences are sparse in presently glaciated regions like Antarctica, models of Antarctic GIA are still uncertain. Although GIA models have been improved to account for regional geological evidence, e.g. IJ05_R2 (Ivins et al., 2013) and W12a (Whitehouse et al., 2012), they still exhibit significant differences (Figure 5.1). The model uncertainties are directly propagated to estimates of the linear trend in present-day ice mass changes and are the major source of errors of this signal component.

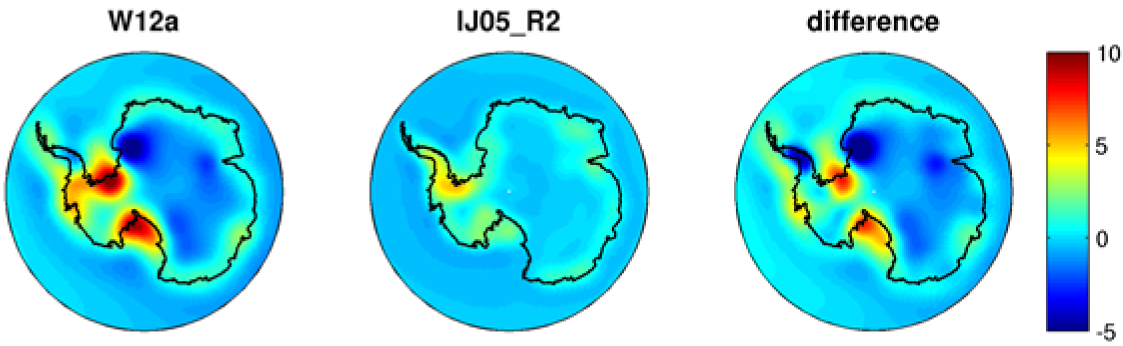

Figure 5.1: GIA-induced present-day crustal deformation rates predicted by the models W12a and IJ05_R2. Right: Differences between both models. Units: mm/yr.

5.2.4 Missing degree one information

Spherical harmonic coefficients of the Earth's gravity field (Stokes coefficients) reflect the combined effect of changes in surface mass and the induced elastic solid Earth deformation. The relation between both contributions is a function of the spherical harmonic degree. For degree one, this relationship also depends on the origin of the chosen reference frame. The reference frame origin realised by GRACE is the centre of mass of the entire Earth (CM). In such a reference frame the Stokes coefficients of the degree one are zero by definition and cannot be separated into their individual contributions (Swenson et al., 2008). Hence, GRACE is insensitive to change in degree one surface mass. Auxiliary data sets are required to avoid the omission of mass changes of degree one.

Different data sets can be used to add degree one information to GRACE monthly solutions. Cheng et al. (2013a) use repeated satellite laser ranging (SLR) observations to derive degree one information from translations of the ground station network. Other approaches combine different types of data like GRACE and ocean models (Swenson et al., 2008), GRACE and assumptions on the passive sea-level fingerprints of land-ice mass change (Sun et al. 2016), or GRACE and sea level anomalies from satellite altimetry (Rietbroek et al., 2016, Uebbing 2022). Time series from these approaches differ both in amplitude and in linear trend (Barletta et al., 2013). All solutions exhibit errors caused by the limitations of the individual utilised techniques. One limitation of all geometric approaches (e.g. using SLR or GPS) is the sparse and irregular distribution of observing stations on the Earth's surface.

5.2.5 Limitations in C20

The flattening of the earth corresponds to the spherical harmonic pattern of the zonal (order zero) coefficient of degree two (C_{20}). Changes in the Earth's dynamic oblateness are related to large-scale mass redistributions and the corresponding changes of the Earth's moments of inertia. For example, long-term changes in C_{20} are mainly caused by GIA, while seasonal variations originate from mass redistributions in the ocean and the atmosphere. These variations are also observed by GRACE and reflected by temporal variations of the degree two and order zero Stokes coefficient. However, GRACE derived estimates of C_{20} exhibit large errors, which are not fully understood but partly caused by residual ocean tide aliasing (Cheng et al., 2013b, Cheng and Ries 2017). Alternative estimates of changes in C_{20} are utilised to replace the original coefficients. The SLR estimates by Loomis et al. (2019, 2020) are widely used, but results from the combination of GRACE and ocean models are available, too (Sun et al., 2016). The effect of an error in the linear trend of the Earth's flattening is largest in polar regions and will bias trends in ice mass change.

5.3 Methodology for determination of error and uncertainty

5.3.1 Noise in monthly gravity field solutions

Instead of using calibrated errors provided by the processing centres, the effect of GRACE errors on regional mass change estimates can also be assessed from the mass change time series (Wahr et al., 2006). For this purpose GRACE errors propagated to the mass changes time series are considered serially uncorrelated. Figure 5.2 illustrates our strategy for assessing GRACE error noise through the example of a mass change time series of the AIS. The time series was derived using a regional integration approach based on tailored sensitivity kernels (cf. ATBD, Groh and Horwath 2019, Döhne et al. 2023).

First, the major long-term and periodic signal components are reduced by means of a linear, periodic and quadratic model. Residuals of the fitted model will still contain both error effects and un-modelled mass changes (e.g. inter-annual mass changes). To remove still present mass signals a high-pass filter based on an 18-month Gaussian average is applied in a second step, where 18 month is the 6-sigma width of the Gaussian weights. The remaining high frequency residuals are used to assess error noise. To infer a single measure for the noise level we calculate its scaled root mean square (rms). Scaling is done to account for the fact that part of the temporally uncorrelated noise content was dampened by the preceding steps of model reduction and high-pass filtering. The scaling factor (1.11) was derived through simulations with random noise time series. The scaled rms of the error noise inferred from the AIS mass change time series given for a specific GMB version and time interval in Table 5.1 is 83 Gt. This estimate may overestimate GRACE errors, since the residuals in fact also contain real signal (Horwath et al. 2012). On the other hand, this estimate disregards possible serial correlations of errors in the GRACE monthly solutions (cf. Horwath & Dietrich, 2009). In addition to GRACE errors, the scaled error rms does also account for those errors caused by residual signal leakage, which have not been removed during the noise estimation procedure. Finally, this estimate is propagated to the formal error of the linear trend. For the entire AIS, this results in a formal error of 2 Gt/yr (Table 5.1).

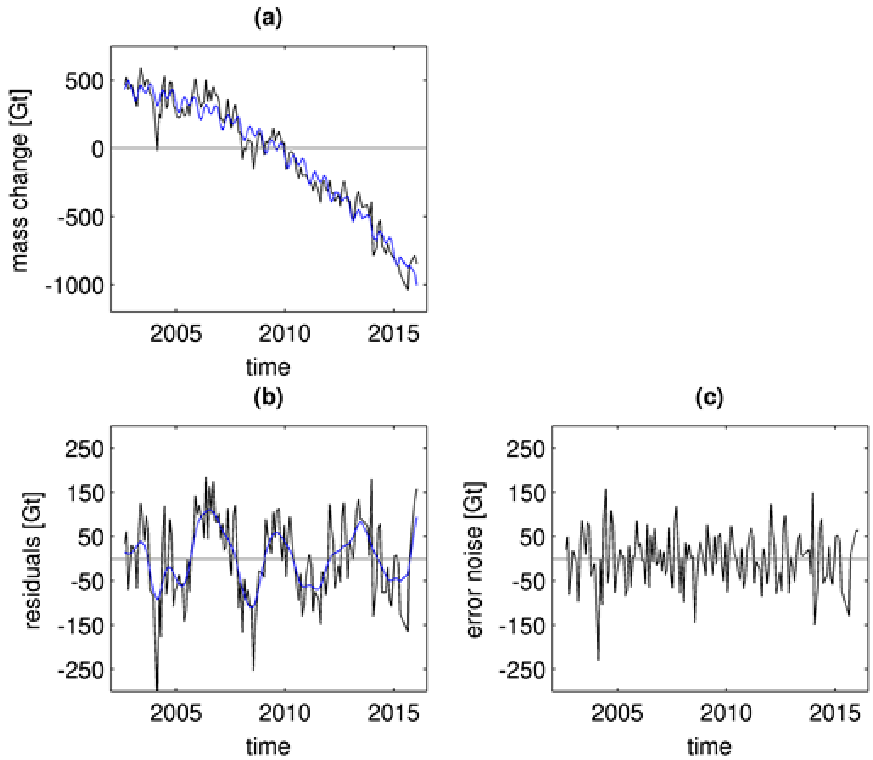

Figure 5.2: Procedure for estimating error noise in mass change time series. (a) Original mass change time series of the Antarctic Ice Sheet (black) and the fitted linear, periodic (1 year, 1/2 year, 161 days) and quadratic model (blue). (b) Mass change residuals (black), i.e. original mass change minus fitted model. Blue line: Low-pass filtered residuals using an 18-month Gaussian average. (c). High-pass filtered residual, i.e. residuals minus low-pass filtered residuals.

5.3.2 Signal leakage

Leakage errors can be assessed by means of high resolution synthetic data sets. The underlying geophysical models should realistically mimic potential sources of leakage, i.e. mass change in different subsystems of the Earth. If mass changes have already been reduced, e.g. during the GRACE de-aliasing process, errors in the applied background models (e.g. AOD1B product) need to be assessed to infer residual leakage signals. Since models often lack error information, uncertainty measures may be derived from a comparison of alternative models. To ensure mass conservation the total change in mass of each synthetic data set needs to be compensated, e.g. by a non-uniform mass change over the ocean following the sea-level equation. After limiting the data sets to the spatial resolution provided by GRACE the algorithm used to derive regional mass changes from GRACE monthly solutions has to be applied to the synthetic data sets. By comparing the synthetic “true” mass changes, derived from the original high-resolution data, with the inferred mass estimates the leakage error can be assessed.

A set of 27 synthetic datasets was used, which mimic AIS mass changes due to SMB fluctuations and due to dynamically induced mass imbalance, residual global oceanic mass variations, as well as far-field mass variations of the Greenland Ice Sheet, the Canadian Arctic and global hydrology (cf. details given by Groh and Horwath 2021). Overall, the simulated leakage effects for the entire AIS are dominated by near-field effects induced by AIS mass changes. The total leakage uncertainty on the linear trend (Table 5.1) is 5 Gt/yr. Note that leakage effects can be more substantial for single basins because in that case, leakage between adjacent basins (such as basin 21 and 22, Thwaites Glacier and Pine Island Glacier) comes into play. See Figure 5.3 as well as Groh and Horwath (2021, Table S1).

5.3.3 GIA

GIA errors in linear ice mass trends are derived by propagating the model uncertainties. Model uncertainties are derived empirically from the spread of a suite of alternative models. The ensemble includes six variants of IJ05_R2 (Ivins et al. 2013) based on different rheologies, three variants of W12a (Whitehouse et al. 2012), namely the preferred variant and the lower and upper bound variants, ICE-6G_D (Peltier et al. 2015, 2018) and the prediction by Caron et al. (Caron et al. 2018), which was derived from a forward model ensemble. By calculating twice the standard deviation of the differences between these model predictions a GIA-induced error in the AIS trend estimate of 34 Gt/yr was derived (Table 5.1).

5.3.4 Missing degree one information

Usually uncertainties of the utilised degree-one time series are based on the intercomparison of different available solutions. By comparing three independent degree one solutions Barletta et al. (2013) have found that for certain drainage basins the error effect on a monthly solution can reach up to 40% of the total monthly error. The degree one contribution to the linear ice mass trend of the entire AIS was found to be 13Gt/yr, mainly originating from GIA. An additional error of the same amount would be introduced by applying a degree one correction which omits linear trends.

Degree-one uncertainties are assessed empirically from the spread of a suite of alternative degree-one time series. This suite comprises an SLR-based record (Cheng et al. 2013a), a time series derived from an inversion approach using satellite gravimetry, GNSS and ocean model data (Rietbroek et al. 2016) and ten realizations of the combination approach (Swenson and Wahr 2008, Sun et al. 2016) used to generate the degree degree-one time series for our study. These variants account for differences in the methodology, GRACE and GRACE-FO solutions series from different processing centres as well as releases (i.e., RL05 and RL06) and GIA models.

By calculating twice the standard deviation of the trends from these time series we assessed the degree-one related uncertainty on the trend for the entire AIS as 21 Gt/yr (Table 5.1).

5.3.5 Limitations in C20

Like for degree one, comprehensive error estimates rely on the intercomparison of various time series for C_{20}. Bloßfeld et al. (2015) have compared different SLR-based results. Solutions differ with respect to the applied processing strategy and the number of SLR satellites used for the analysis. It has been shown that utilising both time series to derive linear ice mass changes for the entire AIS leads to discrepancies of 12Gt/yr.

We account for this potential error source by comparing the trend estimate derived from the C_{20} time series from five different SLR-based time series (Cheng et al. 2013, Bloßfeld et al. 2015, Cheng and Ries 2017, König et al. 2019, Loomis et al. 2019) one combined GRACE/SLR estimate (Bruinsma et al. 2019) and one estimate from a data combination approach (Sun et al. 2016). By calculating twice the standard deviation of the trends from these time series we assessed the C20-related uncertainty on the trend for the entire AIS as 17 Gt/yr (Table 5.1).

5.4 Error and uncertainty documentation

Monthly mass change time series per basin are provided with an average monthly error estimate. This is the scaled error rms, which is a measure for the temporarily uncorrelated noise in each time series caused by GRACE errors as well as residual leakage errors (cf. Section 5.2.1). Using the basin-scale mass change time series, mass balance (i.e. mass change per time) estimates, e.g. linear trends over the entire observational period are also provided. Since effects on the long-term trends are the most critical errors, we pay particular attention to the provision of comprehensive uncertainty estimates for long-term trends. These uncertainties contain the full range of uncertainties affecting the linear trend as described in the previous section. In particular, this comprises the formal error of the linear trend, derived by propagating the scaled error rms, errors caused by GIA model uncertainties, leakage errors from different globally distributed sources, and errors in degree one and C_{20}.

The uncertainty of the mass anomaly of a particular month needs to be expressed as the combined effect of uncertainties of the temporal linear trend, σ^2_{trend}, and the temporally uncorrelated noise, σ_{noise} (cf. Table 5.1). The uncertainties of linear trends are summed up in quadrature from uncertainties due to different error sources. The trend uncertainties are given separately (in the separate file AIS_GMB_trend.dat). In this way, it can be propagated to monthly uncertainties w.r.t. a reference time of the user's choice. The error variance at any epoch is then:

$$\sigma^2_{total}(t) = \sigma^2_{noise} + \sigma^2_{trend}\,(t - t_0)^2.$$

Table 5.1 summarizes the individual error components considered in the total error budget of the MB basin products through the example of the entire AIS. They are an update to the uncertainties quoted by Groh and Horwath (2021), accounting for the extension to GRACE-FO and the consideration of new GRACE/GRACE-FO solution releases. However, the uncertainty budget has not changed dramatically though this update. Groh and Horwath (2021, their Table S1) provide the similar uncertainty budget for each individual drainage basin. Figure 5.3 (taken from Groh and Horwath 2021) illustrates, for each basin, the decomposition of total trend uncertainties into the individual uncertainties sources.

It can be seen that GIA is identified as the dominant error source for many basins and for the big aggregations AIS, EAIS and WAIS. Leakage errors are the dominant error source for the basins of the Amundsen Sea Sector and the Antarctic Peninsula.

Table 5.1: Error components contributing to the overall error budget of the final GMB products for the entire AIS. Values given here are exemplary for the GMB v4.1 for the time interval 2010-01 - 2020-07

Error source	Estimation procedure	Uncertainty
serially uncorrelated noise, mainly due to errors of GRACE solutions		
GRACE solutions	Scaled rms of the error noise, derived from the GRACE time series	83 Gt
Total σ_{noise}		83 Gt
Errors of the linear trend		
GRACE solutions	Propagation of the scaled error rms	2 Gt/yr
GIA model	Intercomparison of different models	32 Gt/yr
Leakage	Simulations with synthetic mass change data	5 Gt/yr
Degree one	Intercomparison of different degree one time series	21 Gt/yr
C20	Intercomparison of different C20 time series	17 Gt/yr

Total σ^2_{trend}	Individual components summed in quadrature	44 Gt/yr

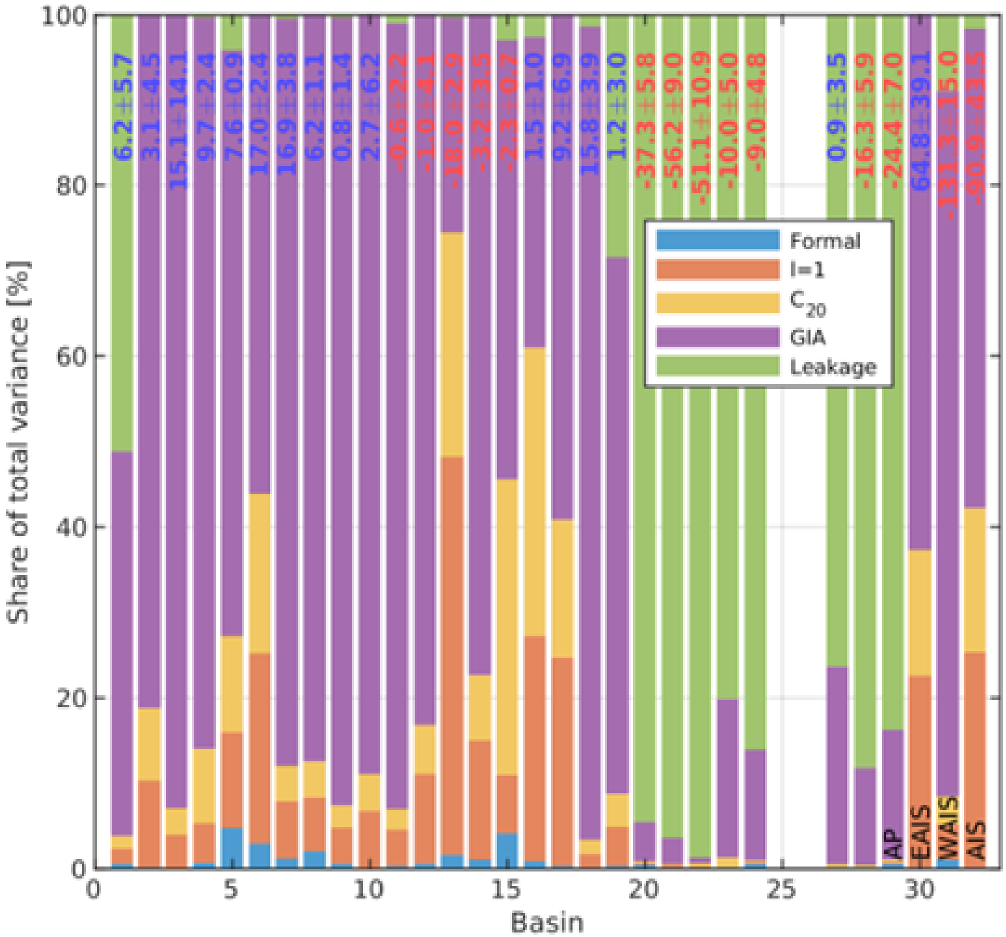

Figure 5.3: Composition, in percentage, of the error variance of each basin (quoted on the top of each bar) from the uncertainty sources (see legend). Reproduction from Groh and Horwath (2021).

5.5 Guideline for using the product

While gridded GMB products can be used to visualise spatial patterns of ice mass changes, most suitable for education and outreach activities, time series of mass changes per basin can be the basis for further analyses and applications. The GMB products of the AIS_cci+ project are provided ready-to-use on the data portal at https://data1.geo.tu-dresden.de/ais_gmb. One possible application would be the combination with modelled basin-averaged variations in SMB to conclude on dynamic mass losses. To solely derive changes in ice mass, superimposed mass signals caused by GIA have been reduced. In case that the users wish to apply an alternative GIA correction, the effect of the applied correction is provided along with the GMB products. In this way users may restore GIA and apply a correction according to their needs.

For each basin, the values for σ^2_{noise} and σ^2_{trend} are provided in the files AIS_GMB_basin.dat and AIS_GMB_trend.dat, respectively. In addition to the official documents provided by the project, a detailed description of the GMB products and the derived error estimates are provided on the data portal.

5.6 References

Barletta, V. R., Sørensen, L. S., & Forsberg, R. (2013). Scatter of mass changes estimates at basin scale for Greenland and Antarctica. The Cryosphere, 7(5), 1411–1432.

Blazquez, A., Meyssignac, B., Lemoine, J. M., Berthier, E., Ribes, A., & Cazenave, A. (2018). Exploring the uncertainty in GRACE estimates of the mass redistributions at the Earth surface: implications for the global water and sea level budgets. Geophysical Journal International, 215(1), 415-430. https://doi.org/10.1093/gji/ggy293

Bloßfeld, M., Müller, H., Gerstl, M., Štefka, V., Bouman, J., Göttl, F., & Horwath, M. (2015). Second-degree Stokes coefficients from multi-satellite SLR. J. Geod., 89(9), 857–871.

Bruinsma, S.; Lemoine, J.M.; Biancale, R.; Valès, N. CNES/GRGS 10-day gravity field models (release 2) and their evaluation. Adv. Space Res. 2010, 45, 587–601. doi:10.1016/j.asr.2009.10.012

Caron, L., Ivins, E. R., Larour, E., Adhikari, S., Nilsson, J., & Blewitt, G. (2018). GIA Model Statistics for GRACE Hydrology, Cryosphere, and Ocean Science. Geophysical Research Letters, https://doi.org/10.1002/2017GL076644

Cheng, M. K., Ries, J. C., & Tapley, B. D. (2013a). Geocenter Variations from Analysis of SLR Data. In Z. Altamimi, & X. Collilieux (Eds.), Reference Frames for Applications in Geosciences (pp. 19–25). International Association of Geodesy Symposia, 138. Springer Berlin Heidelberg.

Cheng, M., Tapley, B. D., & Ries, J. C. (2013b). Deceleration in the Earth's oblateness. JGR. Solid Earth, 118(2), 740–747.

Cheng, M., & Ries, J. (2017). The unexpected signal in GRACE estimates of C_ {20}. Journal of Geodesy, 91:897–91, DOI 10.1007/s00190-016-0995-5

Döhne, T., Horwath, M., Groh, A., & Buchta, E. (2023). The sensitivity kernel perspective on GRACE mass change estimates. Journal of Geodesy, 97(1), 11, https://doi.org/10.1007/s00190-022-01697-8

Flechtner, F., Dobslaw, H., & Fagiolini, E. (2015). AOD1B PDD for Prod Rel 05. GRACE 327-750, Rev. 4.3.

Groh, A., Ewert, H., Rosenau, R., Fagiolini, E., Gruber, C., Floricioiu, D., Abdel Jaber, W., Linow, S., Flechtner, F., Eineder, M., Dierking, W., & Dietrich, R. (2014). Mass, volume and velocity of the Antarctic Ice Sheet: present-day changes and error effects. Surv. Geophys., 35(6), 1481–1505.

Groh, A., Horwath, M., Horvath, A., Meister, R., Sørensen, L. S., Barletta, V. R., Forsberg, R., Wouters, B., Ditmar, P., Ran, J., Klees, R., Su, X., Shang, K., Guo, J., Shum, C. K., Schrama, E., Shepherd, A.2 (2019). Evaluating GRACE Mass Change Time Series for the Antarctic and Greenland Ice Sheet—Methods and Results. Geosciences, 9(10), 415. DOI: 10.3390/geosciences9100415

Groh, A., M. Horwath (2021): Antarctic Ice Mass Change Products from GRACE/GRACE-FO Using Tailored Sensitivity Kernels. Remote Sensing, 13, 1736, https://doi.org/10.3390/rs13091736

Horwath, M., & Dietrich, R. (2009). Signal and error in mass change inferences from GRACE: the case of Antarctica. Geophys. J. Int., 177(3), 849–864.

Horwath, M., Tranchant, J.-B., van den Broeke, M., Legrésy, B. (2012) Evaluation of GRACE monthly solutions of Release 5 versus Rel. 4, with an ice sheet perspective. Proc. GRACE Science Team Meeting, September 2012, Potsdam, Germany.

Ivins, E. R., James, T. S., Wahr, J., O. Schrama, E. J., Landerer, F. W., & Simon, K. M. (2013). Antarctic contribution to sea level rise observed by GRACE with improved GIA correction. J. Geophys. Res. Solid Earth, 118(6), 3126–3141.

König, R.; Schreiner, P.; Dahle, C. Monthly estimates of C(2,0) generated by GFZ from SLR satellites based on GFZ GRACE/GRACE-FO RL06 background models. V. 1.0. GFZ Data Services 2019. doi:10.5880/GFZ.GRAVIS_06_C20_SLR

Loomis, B. D., Rachlin, K. E., & Luthcke, S. B. (2019). Improved Earth oblateness rate reveals increased ice sheet losses and mass-driven sea level rise. Geophysical Research Letters, 46, 6910–6917. https://doi.org/10.1029/2019GL082929

Loomis, B. D., Rachlin, K. E., Wiese, D. N., Landerer, F. W., & Luthcke, S. B. (2020). Replacing GRACE/GRACE-FO with satellite laser ranging: Impacts on Antarctic Ice Sheet mass change. Geophysical Research Letters, 47(3), e2019GL085488.

Peltier, W. R., Argus, D. F., & Drummond, R. (2015). Space geodesy constrains ice age terminal deglaciation: The global ICE-6G_C (VM5a) model: Global Glacial Isostatic Adjustment. J. Geophys. Res. Solid Earth, 120(1), 450–487.

Richard Peltier, W., Argus, D. F., & Drummond, R. (2018). Comment on “An assessment of the ICE-6G_C (VM5a) glacial isostatic adjustment model” by Purcell et al. Journal of Geophysical Research: Solid Earth, 123(2), 2019-2028, http://dx.doi.org/10.1029/2011JB008967

Rietbroek, R., Fritsche, M., Brunnabend, S. - E., Daras, I., Kusche, J., Schröter, J., Flechtner, F., & Dietrich, R. (2012). Global surface mass from a new combination of GRACE, modelled OBP and reprocessed GPS data. J. Geodyn., 59-60, 64–71.

Rietbroek, R., Brunnabend, S. - E., Kusche, J., Schröter, J., & Dahle, C. (2016). Revisiting the contemporary sea-level budget on global and regional scales. Proc. Natl. Acad. Sci. USA, 113(6), 1504–1509.

Schrama, E. J., Wouters, B., & Lavallée, D. A. (2007). Signal and noise in Gravity Recovery and Climate Experiment (GRACE) observed surface mass variations. J. Geophys. Res. Solid Earth (1978–2012), 112(B8).

Seo, K. W., Wilson, C. R., Chen, J., & Waliser, D. E. (2008). GRACE's spatial aliasing error. Geophys. J. Int., 172(1), 41-48.

Sun, Y., Ditmar, P., & Riva, R. (2015). Observed changes in the Earth’s dynamic oblateness from GRACE data and geophysical models. J. Geod., 90(1), 81–89.

Sun Y, Riva REM, Ditmar P (2016) Optimizing estimates of annual variations and trends in geocenter motion and J2 from a combination of GRACE data and geophysical models. J Geophys Res Solid Earth 121(11):8352–8370. https://doi.org/10.1002/2016JB013073

Swenson, S., Chambers, D., & Wahr, J. (2008). Estimating geocenter variations from a combination of GRACE and ocean model output. J. Geophys. Res., B113, B08410.

Uebbing, B. (2022) Consistently closing global and regional sea level budgets. Dissertation, Rheinische Friedrich-Wilhelms-Universität Bonn. https://nbn-resolving.org/urn:nbn:de:hbz:5-68773

Velicogna, I., & Wahr, J. (2013). Time-variable gravity observations of ice sheet mass balance: Precision and limitations of the GRACE satellite data. Geophys. Res. Lett., 40(12), 3055-3063.

Wahr, J., Swenson, S., & Velicogna, I. (2006). Accuracy of GRACE mass estimates. Geophys. Res. Lett., 33, L06401.

Wiehl, M., & Dietrich, R. (2005). Time-variable gravity seen by satellite missions: on its sampling and its parametrization. In Earth Observation with CHAMP (pp. 121-126). Springer Berlin Heidelberg.

Whitehouse, P. L., Bentley, M. J., Milne, G. A., King, M. A., & Thomas, I. D. (2012). A new glacial isostatic adjustment model for Antarctica: calibrated and tested using observations of relative sea-level change and present-day uplift rates. Geophys. J. Int., 190(3), 1464–1482.

6 Ice Shelf CoastLines

6.1 Introduction

The objective of the proposed activity is to investigate the added benefits of combining radar measurements (Sentinel-1) with altimetry (CS2) in the delineation of ice shelf coastlines. This investigation will be conducted over three selected ice shelves (Larsen-C, Ronne, Filchner). Delineation of the Ice Shelf CoastLine (ISCL) will be performed using both SAR images from Sentinel-1 and elevation data from CryoSat-2 altimetry tracks. The elevation data compiled from CS2 tracks will provide an initial guess for the model based on elevation differences that can indicate the start of the ice shelf coastline.

This section will introduce the sources of error and uncertainty throughout the process and how we evaluate, document, and tackle these errors.

6.2 Sources of error

In Table 6.1 likely sources of error are listed. As the DL techniques used require high-quality labels for the data, these need to be considered along with any ameliorations that can be done. Many of these sources of error are already accounted for in the outlined data pipeline presented in the ATBD [AD3], and will be specifically addressed in upcoming experiments.

Table 6.1: Summary of errors and potential solutions.

Type of error	Source of error	Potential solutions	Potential magnitude of error (0=insignificant, 3=large)
IceLine mislabelling	Error is introduced due to the flawed labels since they are generated from a neural network model themselves and not manually delineated	Filtering using CS2 elevation data can catch at least the false positives and remove them from the final output	3
Noisy SAR images	Some errors will be due to the noisy nature of SAR	CS2 data can mitigate that significantly in the areas they exist and mark anchor points to the ISCL	1
Connecting samples	Since the ISCL is delineated separately in each sample, connecting these samples might lead to alignment errors	Enlarging the samples in difficult areas and choosing them to fit in a coherent area	2
Sea Ice	Sea ice can confuse the model in the SAR images and appear as part of the ice shelf or at least blur the exact location of the ISCL	CS2 anchor points can help with that wherever they exist	1
Unmatching S1/CS2 data acquisitions	The model pairs the closest available CS2 to the closest available S1 image (timewise) but that can still be days or even weeks apart which can lead to confusion and error	Minimizing the pairing difference by setting it to be no larger than a certain threshold, but that can be a trade-off between accuracy and time-coverage since setting a specific limit will decrease the time	1

		resolution available in the output data	

6.3 Methodology for determination of error and uncertainty

For determining errors or uncertainty we will reserve a test set of labelled data with which the trained model will be compared. This test set will be held out until the end of the study and used as a diagnostic tool with which to qualitatively evaluate the outputs. The test set will include parts of each ice shelf of the 3 ice shelves proposed in the study. This means that each ice shelf is split into 3 sets: training, validation, and test. Where the test set will only be shown to the model in the error and uncertainty calculation stage.

The F1 score will be used to evaluate the error since it accounts for true positives and negatives and false negatives and positives (since it accounts for both precision and recall) making it a fair estimate of the performance of the model.

Furthermore, a distance map can be used to find the average distance between the predicted and actual ISCL where the error will be the average distance in the resultant distance map. However, since the labelled ISCL is actually an IceLines output rather than the actual ISCL, these metrics might not be accurate on their own since they will produce misleading results in areas where the IceLines labels are faulty. For that, a manual sanity check will be performed as well to give a more realistic metric for the results. That will also evaluate the continuity and the naturalness of the resultant ISCLs since the metrics cannot capture that even if they produce good results.

Finally, confusion matrices will also be produced for each ice shelf and for the overall performance of all ice shelves together to help advance the understanding of the sources of error and identify issues.

6.4 Error and uncertainty documentation

We will be documenting any systemic issues that may exist in the model like weak points and sources of error. The F1 scores and the confusion matrices will be provided for each ice shelf as well as for the aggregate combination of all ice shelves together. Sample images of good, medium and bad performance will also be provided to give a quick view of the performance of the model.

6.5 Guideline for using the product

The output products will consist of monthly ice shelf lines for each of the ice shelves under study. The products will be in the form of GeoPackage vector data (.gpkg) for easy distribution, opening, and size requirements. Each file will contain multiple line strings which hold the data of the line in EPSG:3031 Antarctic Polar Stereographic CRS. The file will also contain metadata containing information related to the Sentinel-1 image used to obtain the line, following the CCI data standard. This data will include acquisition time, ID, mode, polarisation, and processing type. The data will extend from 2017 to 2022 across the Larsen C, Ronne(1 and 2) and Filchner ice shelves. It will have a spatial resolution dependent on the S1 image mode used. Since we are using GRD images, it can reach 20 x 22 for IW and 50 x 50 for EW image modes.

The GeoPackage files produced can be opened and viewed using any software for geographic information including free and open source ones. It can also be opened using common programming languages and packages.